Investigation of $\mathcal{H}_\infty$-Tuned Individual Pitch Control for Wind Turbines

Aoife Henry*[1] | **Manuel Pusch[2]** | **Lucy Pao[1,3]**

[1]Electrical, Computer & Energy Engineering, University of Colorado Boulder, Boulder, CO, USA

[2]Munich University of Applied Sciences, Munich, Germany

[3]Renewable and Sustainable Energy Institute, Boulder, CO, USA

Correspondence

*Aoife Henry, Department of Electrical, Computer, and Energy Engineering, University of Colorado Boulder, Boulder, CO 80309, USA.
Email: aoife.henry@colorado.edu

Abstract

Large wind turbines experience amplified asymmetrical loads at particular harmonics of the rotational frequency. Individual pitch control (IPC) has emerged as a potential controls solution to this problem. $\mathcal{H}_\infty$ control, which facilitates robust, multivariable controller synthesis in the frequency domain, is a candidate approach to IPC design for several reasons. Firstly, the objectives of asymmetrical load attenuation are best described in the frequency domain. Secondly, the IPC control signals and loads in orthogonal directions are coupled, which necessitates a multivariable controller approach. Thirdly, $\mathcal{H}_\infty$ synthesis is a method that can explicitly impose constraints on the robustness of the closed-loop system. A downside of IPC is the significant increase in blade-pitch travel incurred, which introduces additional loading on the blade-pitch bearings over time. We investigate strategies to constrain the blade-pitch travel in the controller tuning procedure. A comprehensive study is thus presented for a range of $\mathcal{H}_\infty$-synthesized IPCs to attenuate asymmetrical loads on large rotors at harmonics of the rotational frequency while mitigating blade-pitch travel. All developed controllers are validated and compared using a 25 MW fixed-bottom offshore wind turbine model via linear analysis of the robustness of the closed-loop system to input and output disturbances and nonlinear analysis via the study of structural load power spectra, damage-equivalent loads (DEL), and the actuator duty cycle (ADC) of the blade-pitch actuator.

KEYWORDS

individual pitch control; robust control; extreme-scale wind turbines; actuator duty cycle; fatigue loading

1 | INTRODUCTION

Wind energy offers enormous potential for renewable energy generation as part of the clean energy transition necessary to reduce the generation of damaging carbon emissions while fulfilling demand for increasing quantities of affordable and reliable energy. The power that can be extracted from a wind turbine scales with the square of the rotor radius (the combined system of the hub and blades). As a consequence of this, there is a strong motivation to produce wind turbines with rotors that span a greater area. A critical limiting factor is the cost of materials. Wind turbine designers are thus faced with a challenge: to produce longer blades with less material. This results in long, slender, and lightweight blades. From a controls perspective, this a) introduces flexible bending modes and b) incurs asymmetrical loads over the significant area spanned by the rotor as a result of the variation in incoming wind. This asymmetrical loading has many contributing sources, including deterministic contributions such as gravity, wind shear, wind veer, tower shadow, yaw/tilt misalignment, and stochastic contributions such as atmospheric turbulence and eddies.[1] The life-cycle of the turbines can be significantly impacted if these loads are not actively alleviated via intentionally-designed control.

Loads experienced by the rotating components (e.g. the blades) of a wind turbine arise at harmonic frequencies of $1P$, $2P$, $3P$, $4P$ (once, twice, three times, four times $p$er revolution) etc. For three-bladed turbines, such as the one under investigation in this work, the loads incurred on the non-rotating components (e.g. the tower) contain harmonics at multiples of three times the rotational frequency i.e. $3P$, $6P$ etc.[2] The "missing harmonics" present on the rotating components appear at their adjacent frequency multiple of $3P$ on the non-rotating components, so $1P$ in the rotating domain is transferred to $0P$ (i.e. zero-frequency

or constant), $2P$ and $4P$ to $3P$, etc.[3] It is therefore possible to project loads experienced by rotating components from the rotating domain (consisting of coordinates for blades 1, 2, and 3) onto a non-rotating domain (consisting of coordinates for the average value c over the blades, loads that contribute to a tilting moment d on the wind turbine structure, and loads that contribute to a yawing moment q on the wind turbine structure) via the Multi-Blade Coordinate (MBC)-transformation, and subsequently to mitigate these transformed loads.[4]

We consider a variable-speed horizontal axis wind turbine (HAWT) (see references for a comprehensive description of HAWT control systems).[5] The control scheme of a wind turbine is typically divided into distinct *control regions* for different wind speeds as shown in Fig. 1. Of interest in this work is *region 3* (R_3), where the wind speed is greater than the rated value, also known as the *above-rated* or *full-load* region. In above-rated conditions, the blade pitch controller is activated to regulate the generator speed to its rated value and the generator torque is controlled to maintain a constant power output.[6]
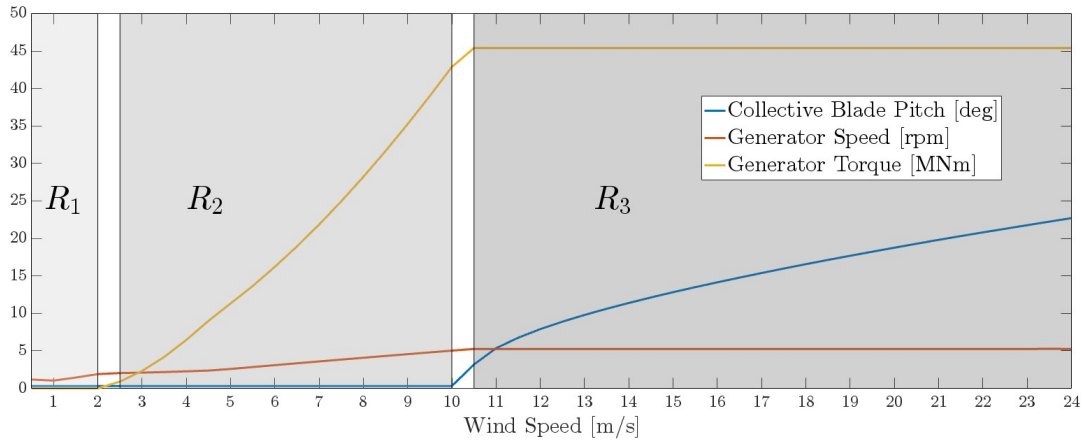

FIGURE 1 Operating regions and steady-state values of the blade-pitch angle β [deg], generator speed ω_g [rpm], and generator torque τ_g [MN·m] for the SUMR wind turbine.[7] Since the gearbox ratio for this turbine model is 1, the rotor speed and generator speed are equivalent.

Blade-pitch control is primarily used for *collective pitch control* (CPC), whereby the rotor speed of a wind turbine is regulated to its rated value in above-rated wind conditions by varying the angle of attack of all three blades identically. The objective of *individual pitch control* (IPC) is to alleviate the asymmetrical loads by superimposing distinct periodic signals onto the collective blade pitch command for each of the blades. Given measurements or estimations of asymmetrical loads (e.g. the blade-root bending moments, tower-top tilting/yawing moments), IPC generates blade pitch signals for each blade of the turbine (see Fig. 2 for a depiction of the blade-pitch control system). Bossanyi et al. develop and validate linear-quadratic-Guassian (LQG)-based and proportional-integral (PI)-structured Coleman transform-based (also known as the MBC transform) IPC to suppress $0P$ loads.[2,8,9] van Engelen proposes integrating additional integral and filtering feedback loops with higher-frequency Coleman transforms to suppress higher harmonic loads with multiple Coleman-transform based controllers.[10,11] A critical cost of implementing IPC is the significant increase in blade-pitch travel, as quantified by the actuator duty cycle (ADC) metric, $ADC = \frac{1}{T} \int_0^T \frac{\dot{\beta}(t)}{\dot{\beta}_{norm}} dt$, where $\dot{\beta}(t)$ is the blade pitch angle rate of change and $\dot{\beta}_{norm}$, defined in Eqn. (1), is its user-specified maximum allowable value.[12]

$$\dot{\beta}_{norm} = \begin{cases} 5°/s & \dot{\beta}(t) \geq 0 \\ -4°/s & \dot{\beta}(t) < 0 \end{cases} \tag{1}$$

Both time-domain and frequency-domain control design approaches have been applied to IPC. Time-domain approaches proposed include model predictive control (MPC),[13,14,15,16] LQG control and linear-quadratic-regulators (LQRs).[17,18,2,19] However, given that the performance specifications of IPC - namely to reduce loads at particular harmonics of the rotational frequency - are best described in the frequency domain, frequency-based approaches have gained popularity in the literature. Furthermore, the robustness of frequency-based approaches can be well described by *robust stability margin* metrics, for which no time-domain equivalent exists. The most established implementation involves transforming rotating blade loads into the tilt
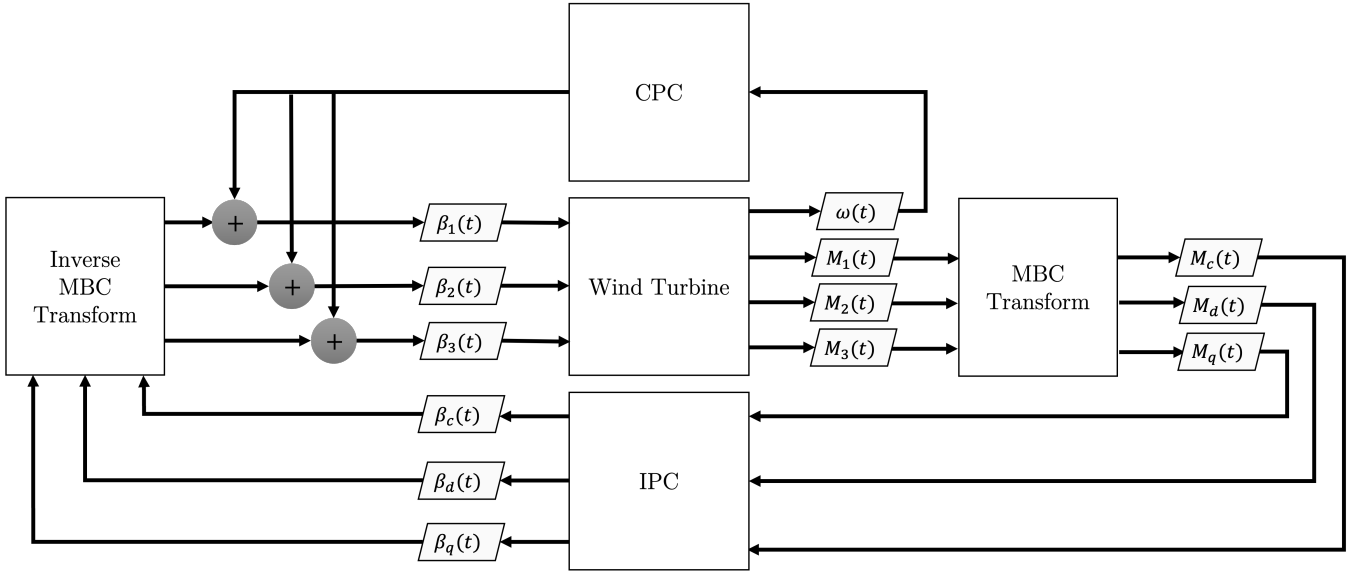
FIGURE 2 Simplified wind turbine system in control loop with collective pitch control (CPC) and individual pitch control (IPC), where ω is the rotor speed [rad/s], $M_{1,2,3}$ are the load signals in the rotating domain, $M_{c,d,q}$ are the MBC-transformed loads in the non-rotating domain, $\beta_{c,d,q}$ are the IPC signals in the non-rotating domain, and $\beta_{1,2,3}$ are the IPC signals in the rotating domain

and yaw coordinates via the MBC transformation, generating IPC signals in these transformed coordinates, and applying the inverse MBC transformation to produce the IPC signals for each blade (see Fig. 2). The controller most often consists of two single-input, single-output (SISO) PI controllers which directly attenuate the $0P$ transformed loads, corresponding to the $1P$ rotating loads.

Alternative transformations have been employed for IPC. One such method is *single-* or *individual-blade control*, whereby the non-inertial reference frame of each blade is compensated for by *fictitious forces* such that each blade can independently regulate its own contribution to the asymmetrical loads experienced by the rotor in response to local blade measurements.[20,21] Another method is the *Clarke transform-based* approach, in which the rotating loads are transformed into orthogonal axes that are stationary with respect to the blades.[3] Approaches that employ trailing edge flaps, rather than IPC, to attenuate asymmetrical loads have also been studied.[22,23,24,25]

A limiting factor of the traditional SISO, MBC-transform based IPC controller is that it neglects the coupling between the tilt and yaw components of the IPC controller inputs (load tracking error) and outputs (individual blade-pitch signals). It has been shown that there does indeed exist a dynamic coupling between tilt and yaw signals in this feedback control.[17,26] Lu et al. derive the MBC transform of a simplified 3-bladed turbine model which establishes that there is a strong coupling between the tilt and yaw components of the IPC inputs and outputs. An important corollary of this fact is that the traditional metrics of gain and phase margin are unreliable measures of robustness for this coupled control system.[27] This supports the development of *multivariable* (i.e. multi-input, multi-output (MIMO)) controllers.

Several works have been published on robust multivariable control for IPC.[28,29] Ossmann et al. design a multivariable linear parameter-varying full-order $\mathcal{H}_\infty$-synthesized controller to attenuate $0P$ and $3P$ loads in the non-rotating frame, and they verify it on a real 2.5 MW wind turbine.[30,31,32] Geyler and Caselitz design two independent, full-order $\mathcal{H}_\infty$-synthesized controllers to a) regulate the rotor speed and active damping of axial tower top oscillations with collective pitch control and b) to suppress the $0P$ loads induced by blade root bending moments with IPC, and they verify the controller on a 1.5 MW turbine model.[26] Lu et al. present a $\mathcal{H}_\infty$-synthesized controller in which a simplified, rigid-blade, blade-decoupled plant is *pre-compensated* with the series combination of a PI controller and $3P$ inverse notch filter to attenuate $0P$ and $3P$ loads.[27] Vali et al. formulate a mixed sensitivity H_∞ optimization problem to solve for an optimal multivariable IPC controller that penalizes control effort using a simplified blade model, and they validate their approach with a 10 MW turbine model.[33]

Challenges that remain in the development of $\mathcal{H}_\infty$-synthesized IPCs are as follows:

- Attenuation of blade-pitch travel is not explicitly considered in the tuning procedure or in the implementation of the controller.
- To the best of the authors' knowledge, all controllers presented to date are tested on wind turbine models of 10 MW capacity or less, which is small relative the largest wind turbines (15 MW) currently commercially available and to even larger wind turbines under development.
- Employing a simplified rigid blade model, as in the case of some previous works, may neglect critical resonant frequencies, particularly for larger wind turbines that are more likely to have slender, flexible blades. [27,33]

In this work, we make the following contributions:

- Development of a framework to tune full-order multivariable $\mathcal{H}_\infty$-synthesized IPCs to mitigate $0P$ and $3P$ loads in the non-rotating (tilt and yaw) domain, corresponding to $1P$ and $2P/4P$ loads in the rotating (blade) domain; tuned for three distinct objectives: robustness, load tracking error minimization, and ADC mitigation.
- Development and validation of three methods for mitigating ADC: a) by *retuning* the $\mathcal{H}_\infty$ synthesized controller for different gains of the weighting function on the control input, b) by using *nonzero references* for the loads that are used as inputs to the controller, and c) by using *finite saturation* of the IPC blade-pitch signals in the rotating domain before passing them to the wind turbine system.
- Linear and nonlinear analysis of all of the above controllers developed in terms of robust stability margins, ADC, DELs, and frequency analysis.

2 | MODELING

2.1 | Plant Model for Nonlinear Simulations

We begin our section on modeling with a description of the nonlinear model used for the simulations, from which the reduced-order linearized model used to tune the controllers is derived. The wind turbine model employed in this work, known as the SUMR, is a 3-bladed, 25 MW turbine with a radius of 171.75 m, rated generator speed of 5.2579 rpm, and rated wind speed of 10 m/s. [7] The reason for this choice of wind turbine model (as compared with more established benchmark models) is that given its blade length, it is considered an *extreme-scale* wind turbine. Wind turbines that span larger rotor areas are more likely to experience problematic asymmetrical loading due to greater differences in incident wind speeds over the greater rotor area. We simulate this turbine using the open-source aero-servo-hydro-elastic wind turbine simulation tool OpenFAST. [34] The model has fourteen degrees-of-freedom, including the first and second flapwise blade modes (three for each blade), the first edgewise blade mode (three for each blade), the generator motion, the first and second fore-aft tower bending modes and the first and second side-to-side tower bending modes.

2.2 | Multi-Blade Coordinate (MBC) Transformation

The *states* of a wind turbine model can be divided into two categories: those associated with rotating components (e.g. blade moments) and those associated with non-rotating components (e.g. yaw bearing or tower base moments). Since there are turbine degrees of freedom that vary with the value of the azimuth angle, θ (defined as the rotational displacement of the first blade from the vertical upward position), when we linearize the model the dependency on θ remains, giving us a *state-dependent* model. The MBC transformation allows us to convert the azimuth-dependent state-space linear model of a three-phase system, such as a 3-bladed wind turbine, into one that is time-invariant for system variations that oscillate three times per full revolution of the azimuth angle. Non-rotating states are unchanged by the transformation, whereas triplets of rotating states associated with the first, second, and third blade are transformed from the rotating domain ($[w_1, w_2, w_3]^T$) to the collective, direct, and quadrature components of the non-rotating domain ($[w_c, w_d, w_q]^T$), where w is the quantity of interest. This tranformation is given by Eqn. (2):

$$T(\theta) = \frac{2}{3} \begin{bmatrix} \overset{\frac{1}{2}}{\cos\left(\theta(t)\right)} & \overset{\frac{1}{2}}{\cos\left(\theta(t) + \frac{2}{3}\pi\right)} & \overset{\frac{1}{2}}{\cos\left(\theta(t) + \frac{4}{3}\pi\right)} \\ \sin\left(\theta(t)\right) & \sin\left(\theta(t) + \frac{2}{3}\pi\right) & \sin\left(\theta(t) + \frac{4}{3}\pi\right) \end{bmatrix} \tag{2}$$

where $\theta(t)$ is defined as the counter-clockwise angle from the vertical upward position to the first blade, such that the non-rotating signals $[w_c, w_d, w_q]^T$, can be computed from their rotating counterparts, $[w_1, w_2, w_3]^T$, for each value of θ as in Eqn. (3):

$$\begin{bmatrix} w_c \\ w_d \\ w_q \end{bmatrix} = T(\theta) \begin{bmatrix} w_1 \\ w_2 \\ w_3 \end{bmatrix} \tag{3}$$

Controllers developed for the MBC-transformed model will output control signals in the non-rotating domain, and so will need to be transformed back into the rotating domain with the inverse MBC-transformation matrix given by Eqn. (4):

$$T(\theta)^{-1} = \begin{bmatrix} 1 & \cos\left(\theta\right) & \sin\left(\theta\right) \\ 1 & \cos\left(\theta + \frac{2}{3}\pi\right) & \sin\left(\theta + \frac{2}{3}\pi\right) \\ 1 & \cos\left(\theta + \frac{4}{3}\pi\right) & \sin\left(\theta + \frac{4}{3}\pi\right) \end{bmatrix} \tag{4}$$

such that the rotating signals for each blade can be computed from their non-rotating counterparts as in Eqn. (5):

$$\begin{bmatrix} w_1 \\ w_2 \\ w_3 \end{bmatrix} = T(\theta)^{-1} \begin{bmatrix} w_c \\ w_d \\ w_q \end{bmatrix} \tag{5}$$

## 2.3 | Linear Parameter-Varying (LPV) Wind Turbine Model for Controller Tuning

$\mathcal{H}_\infty$ control is a linear-control method and we therefore require linear models of our wind turbine system, $G(s)$. To this end, we compute linear state-space matrices of the nonlinear SUMR wind turbine model for a range of above-rated wind speeds (12 - 22 m/s in 0.5 m/s increments) for 36 equidistant azimuth values between $0°$ and $360°$.

The linearizations at each wind speed and azimuth angle result in a *rotational* linear parameter-varying (LPV) model which depends on the azimuth angle, θ, and the mean horizontal wind speed, $\bar{u}_x$. We transform the collection of azimuth-dependent linearizations at each mean horizontal wind speed into the *non-rotating* domain with the MBC transformation matrix given by Eqn. (2) (see references for details on the exact transformation of the state-space matrices).[4] The azimuth-averaged linear models at each wind speed are then linearly interpolated to form a LPV model which depends on mean horizontal wind speed alone, see Eqns. 6. Finally, the model is *reduced* to consider only the relevant control inputs (the IPC commands in the non-rotating domain, β_d and β_q), and measured outputs (the out-of-plane blade-root bending moments in the non-rotating domain, M_d and M_q).

$$\dot{\mathbf{x}} = A(\mathbf{p})\mathbf{x} + B(\mathbf{p})\mathbf{u} \tag{6a}$$

$$\mathbf{y} = C(\mathbf{p})\mathbf{x} + D(\mathbf{p})\mathbf{u} \tag{6b}$$

where $\mathbf{x}$ is the state vector; $\mathbf{y}$ is the output vector, which consists of the out-of-plane blade-root bending moments, M_d and M_q, in the tilt (subscript d) and yaw (subscript q) coordinates, respectively; $\mathbf{u}$ is the control-input vector, which consists of the IPC commands, β_d and β_q, in the tilt and yaw coordinates, respectively; and $A(\mathbf{p}), B(\mathbf{p}), C(\mathbf{p}), D(\mathbf{p})$ are the state-space matrices that depend on the parameter vector, $\mathbf{p}$, which in our case constitutes the low-pass filtered horizontal wind speed incident on the turbine at hub-height. The frequency-response of the resulting MBC transformed and reduced linear wind turbine model is shown in Fig. 3 for several wind speed linearizations.
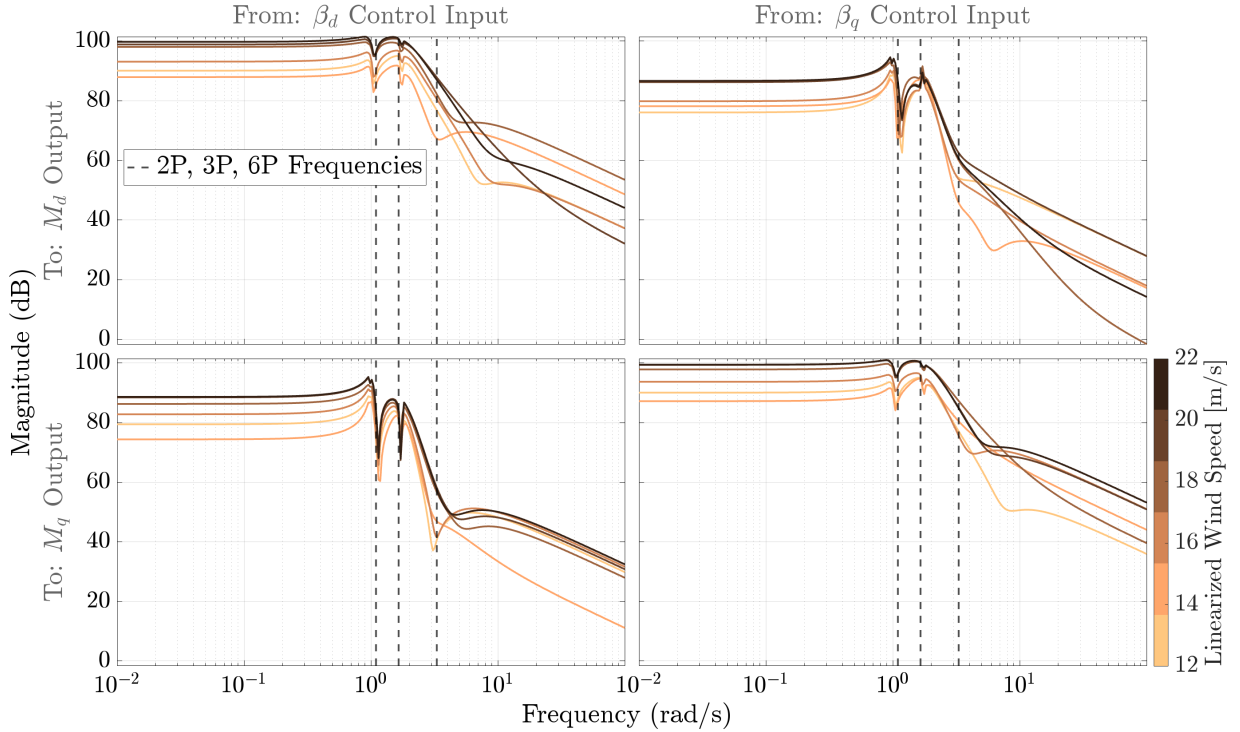
FIGURE 3   Frequency-response of wind turbine model linearized at wind speeds 12, 14, 16, 18, 20, 22 m/s, where darker lines correspond to higher wind speeds, and the vertical dashed black lines correspond to 2*P*, 3*P*, and 6*P* frequencies

3 | ROBUST MULTIVARIABLE CONTROLLER DESIGN

3.1 | Baseline Controller

IPC is commonly implemented by tuning a series interconnection of a notch filter and two PI controllers, which independently regulate the *d* and *q* components of the out-of-plane blade-root bending moments M_d and M_q, respectively. The purpose of the notch filter in the three-bladed turbine case is to filter out the 3*P* content of the M_d and M_q signals, such that the controller can specifically target the 0*P* loads in the non-rotating domain without being excited by 3*P* load signals. The independent regulation is what categorizes this as SISO control, as we effectively have two identical and independent PI controllers, one which reads the tracking error of M_d and generates β_d, and another which reads the tracking error of M_q and generates β_q. These signals are then inverse-transformed into the rotational domain, as per Eqn. (4), and superimposed onto the collective pitch controller for each blade. The gains of the baseline controller, K_0, used in this work are manually tuned to attenuate 0*P* loads, but not to output control signals aggressive enough to result in excessive ADC.

3.2 | Mixed-Sensitivity $\mathcal{H}_\infty$ Controller Synthesis

The objective of $\mathcal{H}_\infty$ control is to find a stabilizing controller K that minimizes the $\mathcal{H}_\infty$-norm of the specified transfer functions, $\frac{\mathbf{z}}{\mathbf{d}}$, where $\mathbf{z}$ is a vector of weighted performance outputs and $\mathbf{d}$ is a vector of the disturbances on the closed-loop system. Both vectors are multiplied by frequency-dependent *weighting functions* that penalize the values of the disturbances and performance outputs to different degrees over specific frequency ranges. It is these weighting functions (W_1, W_2, W_e, and W_u in our case) that are tuned to implement the desired performance specifications for the closed-loop system (see Fig. 4). We consider transfer functions from disturbances at the plant input, $\mathbf{d_1}$, and disturbances at the plant output, $\mathbf{d_2}$, to performance outputs including the weighted control input, $\mathbf{z_u}$, and weighted tracking error, $\mathbf{z_e}$. Given these definitions and the weighting functions, we can derive

the *generalized plant*, P. We select these particular performance outputs because our objective is to attenuate the tracking error, e, at particular harmonics of the rotor rotational speed, and to limit the steady-state value and bandwidth of the control action, **u**. We choose to consider a disturbance at the input, $\mathbf{d_1}$, to impose robustness penalties with respect to uncertainties at the input, and a disturbance at the output, $\mathbf{d_2}$, to include the effect of measurement noise and a reference added to the negative of the plant output in the tuning procedure.

Intuitively, we can think of this optimization problem as minimizing the 'peaks' of various channels in the MIMO transfer function between **d** and **z**. We define these transfer functions based on our desired performance criteria in the frequency domain. Let $F(P, K)$ be the lower *linear fractional transformation* (LFT) of the generalized plant, P, with the controller, K i.e. the closed-loop transfer function from the disturbances, **d**, to the performance outputs, **z**, for a given P and K (see Fig. 4). The ratios between the various weighting functions determine how the various closed-loop transfer functions are penalized in the $\mathcal{H}_\infty$ optimization problem. In the case of *optimal* $\mathcal{H}_\infty$ control, we find all stabilizing controllers, K, that minimize the $\mathcal{H}_\infty$-norm of $F(P, K)$, given by Equation (7). [29]

A more attainable *sub-optimal* controller can be generated by finding all stabilizing controllers, K, such that $\|F(P, K)\|_\infty < \gamma$, $\gamma > \gamma_{\min}$, where γ is a given upper threshold value for the $\mathcal{H}_\infty$-norm of $F(P, K)$. *Mixed-sensitivity* $\mathcal{H}_\infty$ control is a closed-loop shaping method, in which we shape one or more closed-loop transfer functions by minimizing the $\mathcal{H}_\infty$ norm of the relevant stacked transfer functions $\frac{\mathbf{z}}{\mathbf{d}}$.

$$\|F(P, K)\|_\infty := \begin{cases} \max\limits_{d(t) \neq 0 \in L_2} \frac{\|z(t)\|_2}{\|d(t)\|_2} & \text{in the time domain} \\ \max\limits_{\omega} \overline{\sigma}(F(P, K)(j\omega)) & \text{in the frequency domain} \end{cases} \tag{7}$$

where $\|x(t)\|_2 := \sqrt{\int_0^\infty \sum_i |x_i(t)|^2 \, dt}$ is the 2-norm of the time-domain vector signal, x, and $\overline{\sigma}(F(P, K)(j\omega))$ is the maximum singular value of $F(P, K)$ at frequency ω.

In this work we develop a *full-order* multivariable controller, K, that considers the measured and MBC-transformed out-of-plane blade-root bending moments $[M_d, M_q]^T$ as inputs, and outputs IPC commands in the non-rotating domain $[\beta_d, \beta_q]^T$. The full-order controller is a transfer function with the same number of states as the *generalized plant*, P, used for tuning (see Fig. 4), which thus poses a convex optimization problem for $\mathcal{H}_\infty$-synthesis. [29]

3.3 | Frequency-Domain Performance Specifications

We can express the performance specifications of our controller as frequency-dependent constraints on one or more of the following closed-loop transfer functions:

- The *output sensitivity function*, $S_o = (I + GK)^{-1}$, is the closed-loop transfer function from the weighted output disturbances, $\mathbf{d_2^w}$, to the tracking error, **e**. This determines the *disturbance rejection* properties of the closed-loop system. In our case, the upper bound of S_o controls how the deviation of $[M_d, M_q]^T$ from their (nominally zero-valued) references, $[M_d^\star, M_q^\star]^T$, respond to measurement noise, nonzero references or disturbances on these load measurements due to the wind. In particular, we want to ensure that the loads oscillating at $0P$ and $3P$ frequencies in the non-rotating domain are attenuated with respect to wind disturbances that incur these asymmetrical loads.

- The *input sensitivity function*, $S_i = (I + KG)^{-1}$, is the closed-loop transfer function from the weighted input disturbance, $\mathbf{d_1^w}$, to the perturbed control action, $\tilde{\mathbf{u}}$. This determines a) the size and bandwidth of the control input, which in our case is the vector of IPC commands, $[\beta_d, \beta_q]^T$, and b) the robust stability with respect to disturbances on the input and to additive plant modeling uncertainty. [29] The upper bound of KS_o limits the magnitude of $[\beta_d, \beta_q]^T$ at zero-frequency and the magnitude of $[\dot{\beta}_d, \dot{\beta}_q]^T$ in the higher-frequency range.

- The *complementary input sensitivity function*, $T_i = KG(I + KG)^{-1}$, is the negative of the closed-loop transfer function from the weighted input disturbance, $\mathbf{d_1^w}$, to the unperturbed control action, **u**.

- The *control sensitivity function*, $KS_o = K(I + GK)^{-1}$, is the negative of the closed-loop transfer function from the weighted output disturbance, $\mathbf{d_2^w}$, to the unperturbed control action, **u**. Note that this is mathematically equivalent to S_iK.

- The *disturbance sensitivity function*, $GS_i = G(I + KG)^{-1}$, is the closed-loop transfer function from the weighted input disturbance, $\mathbf{d_1^w}$ to the unperturbed plant output, **y**. Note that this is mathematically equivalent to S_oG.
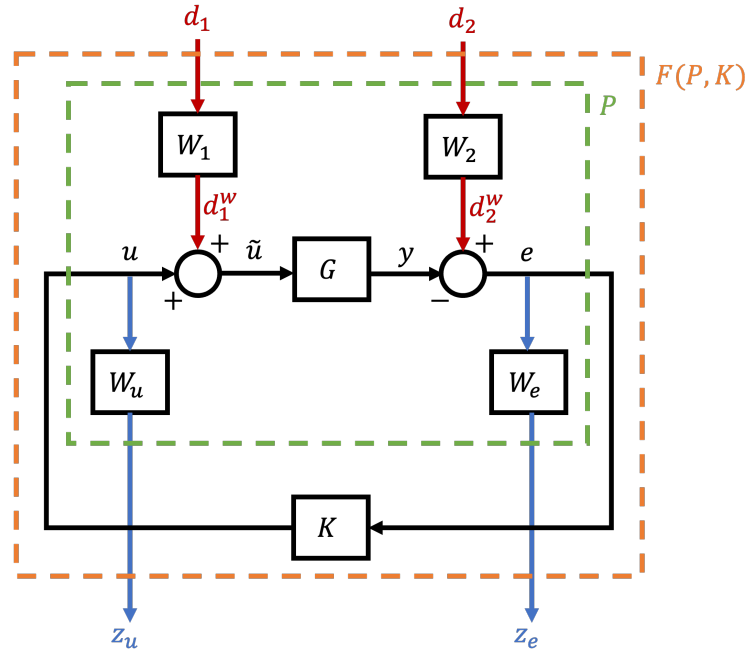
FIGURE 4 Closed-Loop System of Generalized Plant, P, and Controller K

3.3.1 | Generalized Plant

We derive the *generalized plant* shown in Fig. 4 by defining the disturbances, $\mathbf{d_1}, \mathbf{d_2}$, and the performance outputs $\mathbf{z_u}, \mathbf{z_e}$. The disturbances represent external signals that can perturb internal ones, where $\mathbf{d_1}$ represents a disturbance on the control input and $\mathbf{d_2}$ represents a reference signal, high-frequency measurement noise, or a low-frequency disturbance on the output. These are weighted by *input weighting functions* W_1 and W_2 to generate $\mathbf{d_1^w}$ and $\mathbf{d_2^w}$. The performance outputs are particular signals of importance that are transformed by *output weighting functions*, where $\mathbf{z_u}$ is the control input signal, $\mathbf{u}$, weighted by W_u, and $\mathbf{z_e}$ is the tracking error, $\mathbf{e}$, weighted by W_e. We also consider the input and output signals for the controller, $\mathbf{e}$ and $\mathbf{u}$, respectively. The linear wind turbine plant used, G, corresponds to the nonlinear model linearized at 16 m/s, MBC-transformed and averaged over all azimuth angles (see Sec. 2). We can express the relationship between these signals with the generalized plant transfer function P by finding the expressions for each of the performance outputs, $\mathbf{e}$ and $\mathbf{u}$, in terms of the disturbances, $\mathbf{d_1}$ and $\mathbf{d_2}$:

$$\mathbf{u} = K(W_2\mathbf{d_2} - G(W_1\mathbf{d_1} + \mathbf{u}))$$
$$\Rightarrow \mathbf{u} = -T_i W_1\mathbf{d_1} + KS_o W_2\mathbf{d_2} \tag{8a}$$

$$\mathbf{e} = W_2\mathbf{d_2} - G(W_1\mathbf{d_1} + Ke)$$
$$\Rightarrow \mathbf{e} = -GS_i W_1\mathbf{d_1} + S_o W_2\mathbf{d_2} \tag{8b}$$

We can then derive expressions for the weighted performance outputs as a function of the disturbances to get the LFT of the generalized plant, $F(P, K)$:

$$\begin{bmatrix} \mathbf{z_u} \\ \mathbf{z_e} \end{bmatrix} = \underbrace{\begin{bmatrix} W_u & 0 \\ 0 & W_e \end{bmatrix} \begin{bmatrix} -T_i & KS_o \\ -GS_i & S_o \end{bmatrix} \begin{bmatrix} W_1 & 0 \\ 0 & W_2 \end{bmatrix}}_{F(P,K)} \begin{bmatrix} \mathbf{d_1} \\ \mathbf{d_2} \end{bmatrix} \tag{9}$$

Including the controller K, inputs $\mathbf{u}$, and tracking error $\mathbf{e}$, we get the expression for the generalized plant P:

$$\begin{bmatrix} \mathbf{z_u} \\ \mathbf{z_e} \\ \mathbf{e} \end{bmatrix} = \underbrace{\begin{bmatrix} W_u & 0 & 0 \\ 0 & W_e & 0 \\ 0 & 0 & I \end{bmatrix} \begin{bmatrix} 0 & 0 & I \\ -G & I & -G \\ -G & I & -G \end{bmatrix} \begin{bmatrix} W_1 & 0 & 0 \\ 0 & W_2 & 0 \\ 0 & 0 & I \end{bmatrix}}_{P} \begin{bmatrix} \mathbf{d_1} \\ \mathbf{d_2} \\ \mathbf{u} \end{bmatrix} \tag{10}$$

Inserting the generalized plant P into a closed-loop system with the controller, we get the block diagram in Fig. 4.

3.3.2 | Weighting Functions

The weighting functions in Fig. (4) are designed to set frequency-dependent penalties on the different transfer functions in the optimization problem. Eqn. (9) shows which transfer functions are influenced by each.

We set the disturbance weighting functions as identity functions weighted by gains A_{W_1} and A_{W_2}:

$$W_1 = A_{W_1}\mathbf{I_2} \tag{11a}$$

$$W_2 = A_{W_2}\mathbf{I_2} \tag{11b}$$

We set the weighting function, W_e, associated with the tracking error to be a low-pass filter in series with an inverse notch filter for the purposes of penalizing the 3P frequency ω_{3P}, together with a gain A_{W_e}. The inverse of W_e serves as an upper bound on the closed-loop transfer functions S_o and GS_i and so the low-pass filter will penalize gains at the 0P frequency, and the inverse notch filter will penalize gains at the 3P frequency. The constant $\overline{g}$ determines the gain of the filter at frequency ω_{3P} and the width of the filter correlates positively with the damping factor, ζ. We set the weighting function, W_u, associated with the control inputs to be a high-pass filter together with a gain A_{W_u}. The inverse of W_u serves as an upper bound on the closed-loop transfer functions T_i and KS_o, and so the high-pass filter will penalize actuator activity at high frequencies.

$$W_u = A_{W_u} \frac{1}{\epsilon_u} \frac{s + \frac{\omega_u}{M_u}}{s + \frac{\omega_u}{\epsilon_u}} \mathbf{I_2}, M_u = 2, \epsilon_u = 0.001M_u, \frac{\omega_u}{M_u} = 0.75\omega_{3P} \tag{12a}$$

$$W_e = A_{W_e} \frac{1}{M_e} \frac{s + M_e\omega_e}{s + \epsilon_e\omega_e} \frac{s^2 + 2\overline{g}\zeta\omega_{3P}s + \omega_{3P}^2}{s^2 + 2\zeta\omega_{3P}s + \omega_{3P}^2} \mathbf{I_2}, M_e = 5, \epsilon_e = 0.05, \epsilon_e\omega_e = 0.005\omega_{1P}, \zeta = 0.01, \overline{g} = 15 \tag{12b}$$

where $\frac{1}{\epsilon_u}$ controls the gain of W_u at high frequencies; $\frac{\omega_u}{M_u}$ is the breakpoint frequency of the high-pass filter in W_u and is chosen to be a fraction of the 3P frequency, ω_{3P}; $\frac{1}{M_e}$ controls the gain of W_e at low frequencies; and $\epsilon_e\omega_e$ is the breakpoint frequency of the low-pass filter in W_e and is chosen to be a small fraction of the 1P frequency, ω_{1P}.

Note that it is not the absolute amplitudes of A_{W_1}, A_{W_2}, A_{W_e}, and A_{W_u} that matter, but rather their *relative* amplitudes. This determines the relative significance of penalties on particular transfer functions. The precise best values depend on the goals of the controller (i.e. whether disturbances on the output pose a greater threat to stability than disturbances on the input, or whether we have reason to place a higher penalty on actuator activity than on tracking error) and also on the scaling used for the plant G.

We initially perform a sweep over the gains A_{W_2}, A_{W_e}, and A_{W_u} (setting A_{W_1} to a constant value of 1, since it is the ratios between these gains that matter), generating a controller via $\mathcal{H}_\infty$-synthesis and performing nonlinear simulations in OpenFAST for each set, to find sets of weighting function gains that result in three distinct controllers: a) one that maximizes robustness, K_{rob} (in terms of the greatest multi-loop disk margin, see Sec. 4.3), b) one that minimizes actuator activity, K_{adc} (in terms of the least ADC), and c) one that minimizes the load tracking error, K_{err} (in terms of the least root mean-squared error (RMSE) of the out-of-plane blade-root bending moment, M_1). Table 1 shows the sets of weighting function gains found for each objective and Fig. 5 compares the frequency response of the resulting weighting functions. Note that the set of gains resulting in controllers with high robustness and controllers with low ADC are equivalent, and will henceforth be referred to as K_{adc} for brevity. The results of this sweep in Table 1 and Fig. 5 suggest that a significantly greater weighting ought to be placed on the output disturbance (greater A_{W_2}) and on the tracking error (greater A_{W_e}) in order to mitigate load tracking error, as compared with the goal of attenuating ADC. The middle plot of Fig. 5 illustrates the weighting placed on low frequencies ($\approx 10^{-5}$ rad/s or lower) and on the 3P frequency (1.6518 rad/s) by the low-pass filter and inverse-notch filter terms in W_e, respectively. In comparison, the right plot of Fig. 5 illustrates the weighting placed on high frequencies ($\approx 10^5$ rad/s or higher) by the high-pass filter term in W_u.
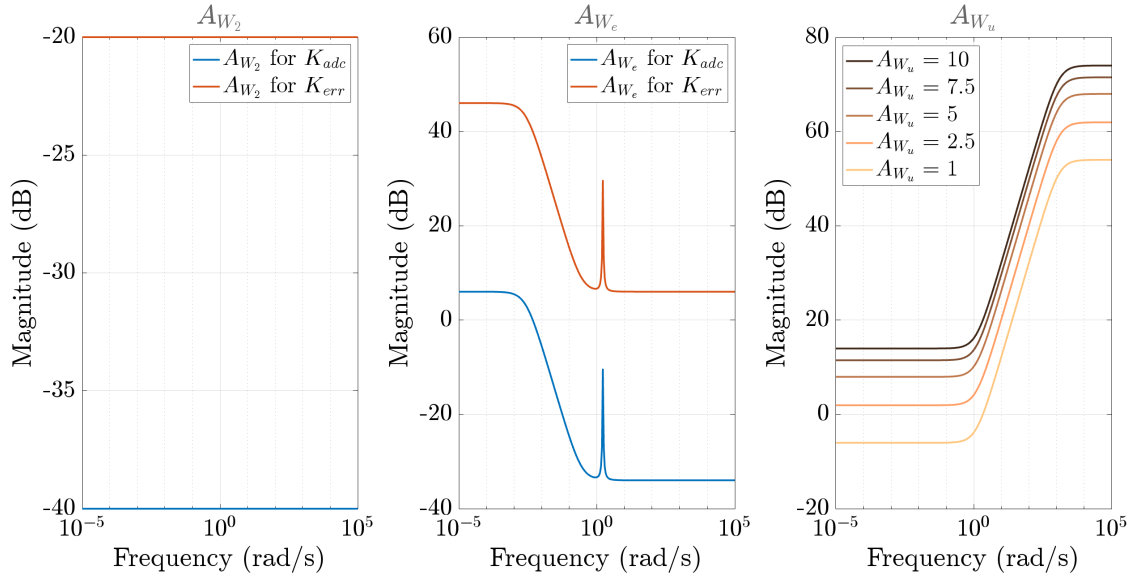
FIGURE 5 Frequency-response of weighting functions for different weighting gains $A_{W_2}, A_{W_e}, A_{W_u}$, where blue and red lines correspond to the weights used for K_{adc} and K_{err}, respectively. On the rightmost plot, the sweep of weighting function gains A_{W_u} tested to mitigate ADC in all controllers is shown, where darker colors correspond to increasing values of A_{W_u}.

See Fig. 6 for a visualization of the variation in multi-loop disk margin, ADC, and M_1 RMSE as individual weighting gains are increased. Note that the robustness and tracking error tend to fall while ADC tends to rise with increased emphasis on the tracking error (increased A_{W_e}), and vice-versa with increased emphasis on the actuator activity (increased A_{W_u}). Since the fundamental gains of W_1 and W_2 (before amplification with A_{W_1} and A_{W_2}) are low relative to those of W_e and W_u, relative changes in A_{W_2} do not play a significant role on the controller robustness, actuator activity, or tracking error.
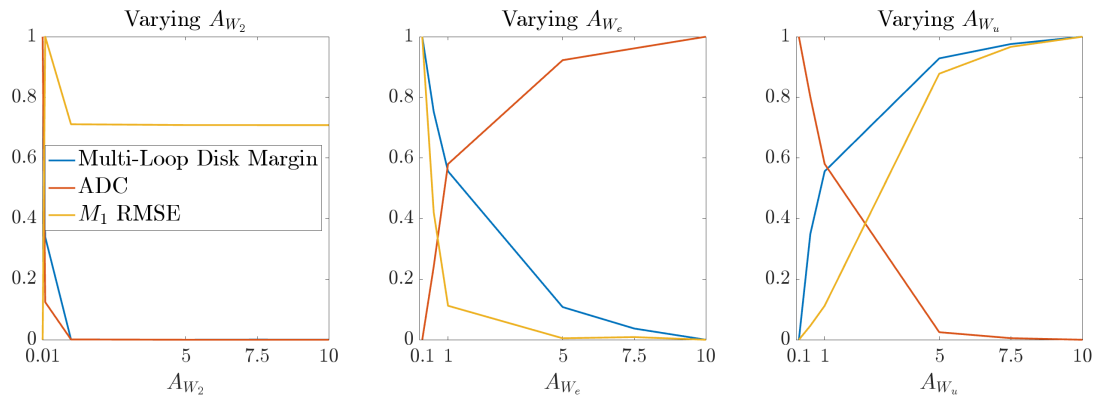
FIGURE 6 Normalized (between 0 and 1) multi-loop disk margin, ADC, and M_1 RMSE values vs. variation in each of the weighting gains $A_{W_2}, A_{W_e}, A_{W_u}$, where all but one is held constant in each plot. Note that since the quantities are normalized for each plot such that all three lines are visible, the effect of variation in different weighting function gains is not comparable here. In reality, variation in the gains A_{W_e} and A_{W_u} relative to each other are much more significant.

T A B L E 1 Sets of weighting function gains that result in the most robust controller, K_{rob}, the controller incurring the least ADC, K_{adc}, and the controller resulting in the least load tracking error, K_{err}, compared to the baseline SISO PI controller, K_0, and the open-loop case (for which no closed-loop stability margins can be computed).

Case Description	Multi-Loop Disk Margin [-]	ADC [-]	M_1 RMSE [kNm]
Baseline Controller, K_0	0.827	0.141	29868
Open-Loop (no IPC)	-	0.026	33572
Robust Controller, K_{rob}, $A_{W_1} = 1, A_{W_2} = 0.01, A_{W_e} = 0.1, A_{W_u} = 10$	1.912	0.028	33116
ADC Controller, K_{adc}, $A_{W_1} = 1, A_{W_2} = 0.01, A_{W_e} = 0.1, A_{W_u} = 10$	1.912	0.028	33116
Error Controller, K_{err}, $A_{W_1} = 1, A_{W_2} = 0.1, A_{W_e} = 10, A_{W_u} = 7.5$	0.768	0.244	27596

3.4 | Blade-Pitch Travel Attenuation

In order to limit the ADC of the blade-pitch actuation, we experiment with three methods: a) *retuning* the $\mathcal{H}_\infty$-synthesized controller for increasing control input weighting function gains, A_{W_u}, b) implementing a range of *nonzero reference* values for the d component of the transformed blade-root bending moment, $M_d^\star$, and c) implementing a range of *finite saturation* values for the IPC signals output from the controller and transformed back into the rotating domain, $\overline{\beta}_1$. All three approaches should result in attenuation of the amplitude of the sinusoidal IPC commands and may have some negative impact on the robustness and/or load attenuation properties of the controller.

The sweep of nonzero references $M_d^\star$ tested are computed as percentages of the mean value of M_d in the open-loop case, $\underline{M_d}$, over all wind fields used in the simulations. The reasoning for only varying the d reference is due to the effect of wind shear, because as a consequence d loads will generally be greater than q loads and the mean value of M_d will generally be nonnegative without control. This means that we can safely choose a nonnegative value for $M_d^\star$ for the controller to steer the wind turbine towards from above. See the upper plot of Fig. 7 for the reference values $M_d^\star$ superimposed on a sample M_d time-series.

The sweep of finite saturation values $\overline{\beta}_1$ are computed as percentages of the mean values of β_1 in the closed-loop case for a $\mathcal{H}_\infty$-synthesized controller, $\underline{\beta}_1$, over all wind fields used in the simulations. Since the output for all three blades are identical other than the 120° phase-shift between them, we can safely use the mean value from blade 1, $\underline{\beta}_1$, as a basis for saturating all three blades. See the lower plot of Fig. 7 for the positive saturation values $\overline{\beta}_1$ superimposed on a sample β_1^{ipc} time-series, where β_1^{ipc} is the inverse-MBC-transformed IPC signal for blade 1 before it is added to the CPC signal.

4 | LINEAR ANALYSIS

4.1 | Frequency Response of Tuned Controllers

Fig. 8a shows the frequency response of the $\mathcal{H}_\infty$-synthesized controllers for the set of weighting function gains corresponding to high robustness, K_{rob}, and low ADC, K_{adc}, (recall that the best-performing set of weighting function gains for both are found to be identical, see Sec. 3.3.2). Fig. 8b is the equivalent plot for the controllers tuned for the set of weighting function gains corresponding to low M_1 RMSE, K_{err}. Each are plotted for the range of A_{W_u} values tested in the 'retuning' approach to constraining ADC. The dotted blue line shows the frequency response of the baseline SISO PI controller for comparison. Comparing the two plots, we can see that K_{err} is a more aggressive controller than K_{adc} (i.e. produces higher gains) and also that it presents a more significant peak at 3P. In comparison K_{adc} presents approximately equivalent peaks at 2P and 3P frequencies, with another more rounded peak at 6P. Note that both controllers have off-diagonal-components from the M_q tracking error to the β_d control input as well as from the M_d tracking error to the β_q control input that are close in amplitude to the diagonal components, reinforcing the motivation for such multivariable controllers.

4.2 | Frequency Response of Closed-Loop Transfer Functions

Sec. 3.3 describes the closed-loop transfer functions that are shown in Eqn. (9) and for which $\|F(P, K)\|_\infty$ is minimized in the $\mathcal{H}_\infty$ optimization problem. Fig. 9 visualizes the magnitude of the frequency response for the $d - d$ channel of these transfer functions multiplied by the associated input weighting function for the tuned K_{adc} and K_{err} controllers which result in the lowest ADC and lowest M_1 RMSE in nonlinear simulations, respectively (solid lines). The dashed lines show the inverse penalty placed
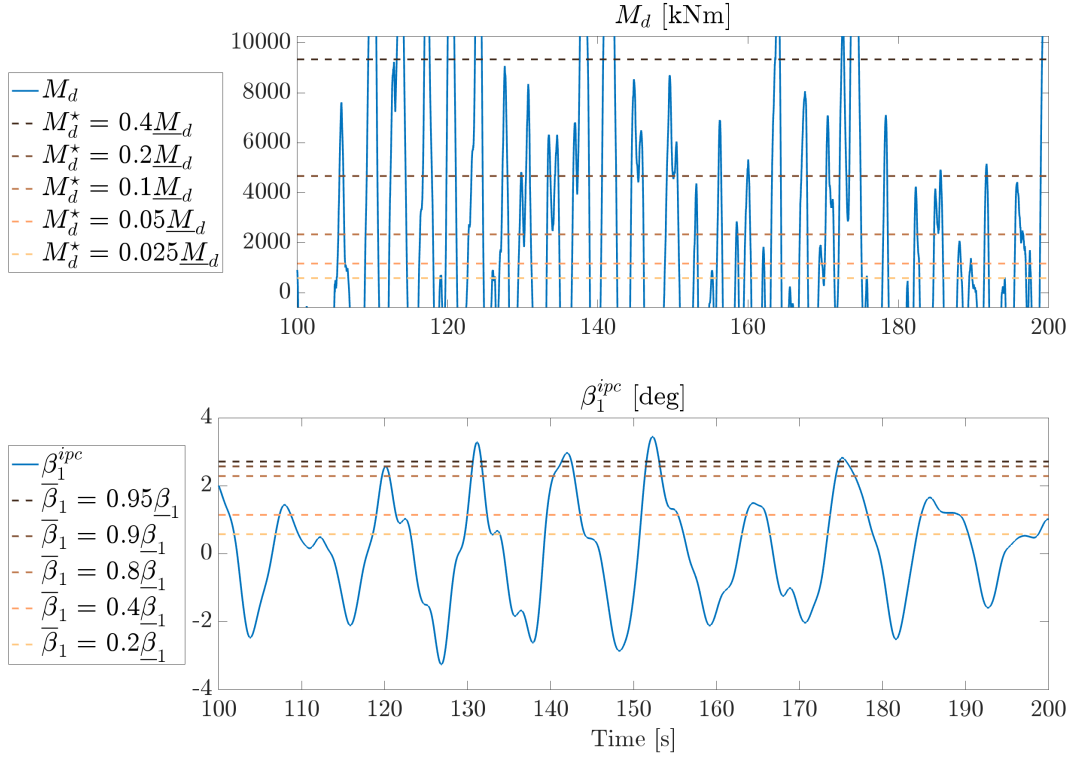
FIGURE 7 Time-series plot of the reference values $M_d^\star$ superimposed on a sample M_d time-series (top) and positive saturation values $\overline{\beta}_1$ superimposed on a sample β_1^{ipc} time-series (bottom). Note that we have magnified the top plot such that the reference values are visible.

on these transfer functions by the product of the inverse of the associated output weighting functions and minimum value of $\|F(P,K)\|_\infty$ achieved by the $\mathcal{H}_\infty$ optimization problem, γ. The bottom two plots, for the disturbance sensitivity GS_i and the output sensitivity S_o, show the open-loop (no IPC) equivalents (black dotted lines) that we can compare to. It is clear that the GS_i and S_o transfer functions are altered from the open-loop case for the K_{adc} controller at lower frequencies ($\approx 0P$) and $3P$ frequencies, while the closed-loop and open-loop lines converge at higher frequencies. This tells us that it is these transfer functions that are the limiting factor (i.e. the $\mathcal{H}_\infty$-norm 'peak' that is minimized over all transfer functions) in the optimization of K_{adc}. In contrast, GS_i and S_o are almost unchanged from the open-loop case for K_{err}, whereas T_i and KS_o are notably different compared to the K_{adc} equivalents. This suggests that it is these transfer functions that are the limiting factor in the tuning of K_{err}.

4.3 | Measures of Robustness

The purpose of a robust control method such as $\mathcal{H}_\infty$-synthesis is to design a controller for a given system that meets stability and performance requirements, even in the presence of uncertainties in the system model and/or exogenous disturbances. To this end, we need a measure of how much perturbation to the gain and/or phase of the various loops of the system ($d-d$, $d-q$, $q-d$ or $q-q$, perturbed either individually or simultaneously) would result in instability of the closed-loop system. In this section we define the metrics used in this work to describe these *robust stability margins*.

Loop-at-a-time disk margins can be visualized as a disk-shaped region of stability such that if any complex-valued perturbation selected from this disk were applied to an individual channel in the closed-loop system, with all remaining loops closed, it would remain stable. This addresses the question of simultaneous gain and phase variations neglected by classical gain/phase margins and so is a more conservative measure, although it does not address the interaction of individual loops in a MIMO system.

Multi-loop disk margins describe the disk-shaped region of stability such that if any independent x number of complex-valued perturbations were selected from this disk and applied to the x number of loop channels under consideration, with all
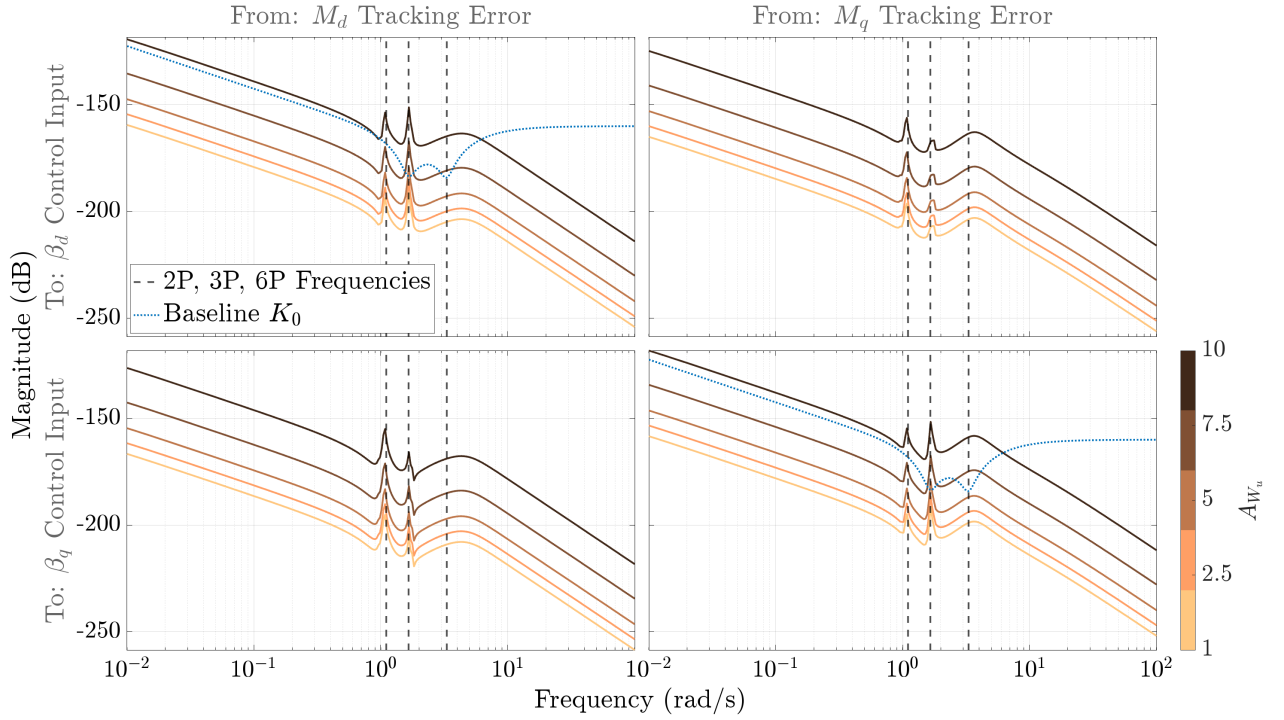
(a) Controller tuned for high robustness and low ADC (equivalent): K_{rob}, K_{adc}
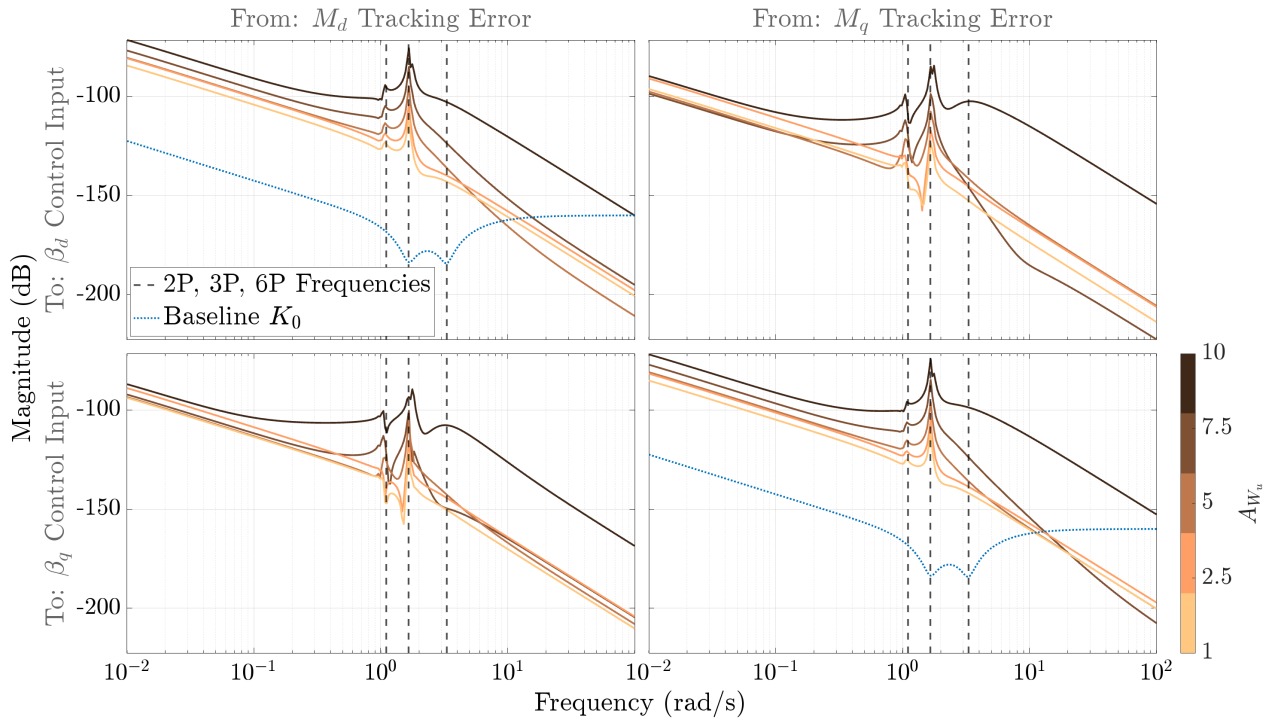
(b) Controller tuned for low M_1 RMSE, K_{err}

FIGURE 8 Frequency response for K_{adc} and K_{err}, tuned with wind turbine model linearized at 16m/s, for varying gains of W_u (black corresponding to the highest gain with lighter colors corresponding to decreasing gains). Note the peaks at the 2P, 3P and 6P frequencies.
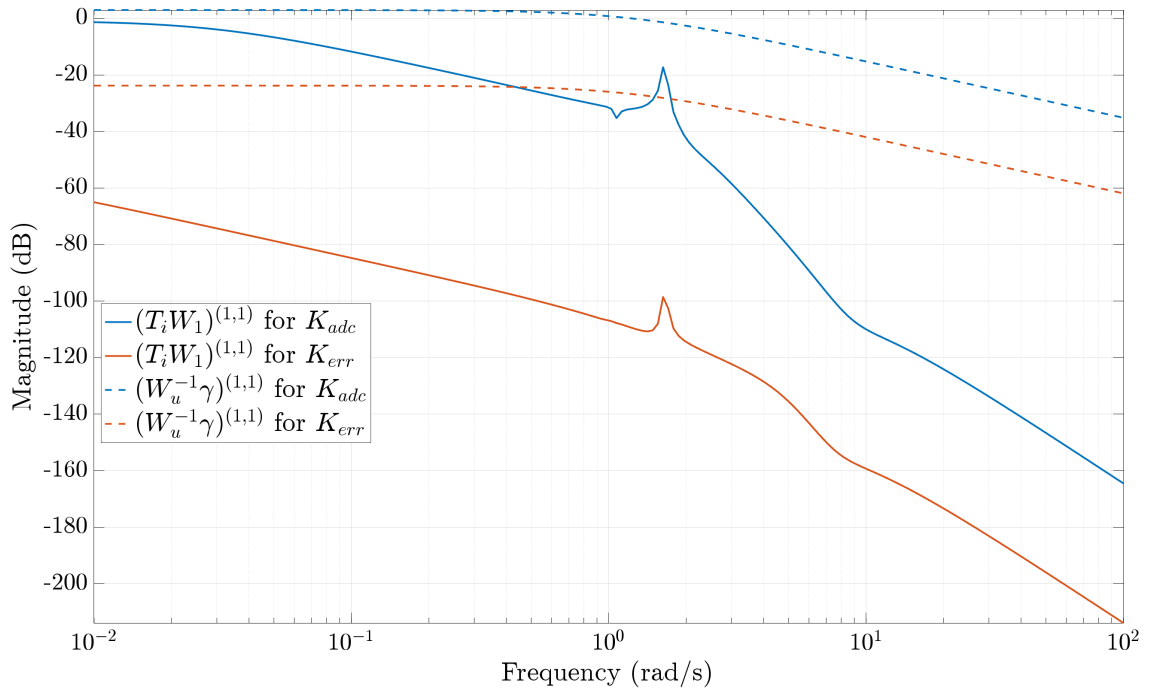
(a) $T_i^{(1,1)} = \frac{z_{u,d}}{d_{1_d}}$
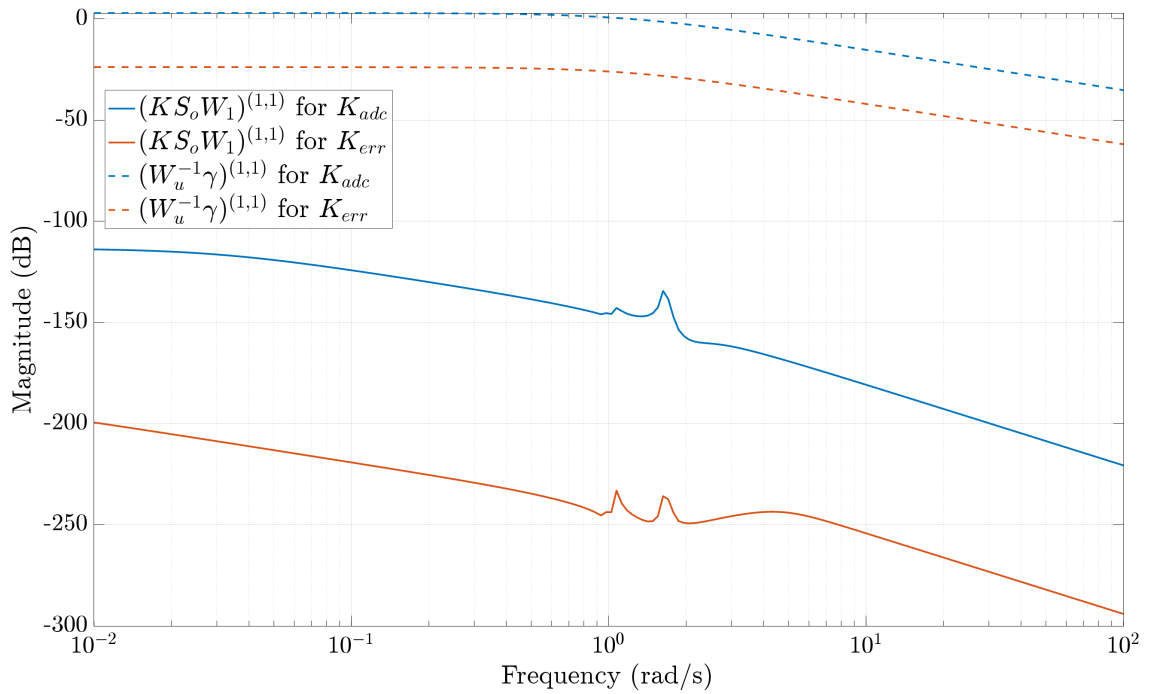

(b) $KS_o^{(1,1)} = \frac{z_{u,d}}{d_{2_d}}$

remaining loops closed, the closed-loop system would remain stable. We could measure *multi-loop input disk margins* by injecting independent perturbations at all inputs to the plant if we wish to estimate the robustness to uncertainties at the inputs,

(c) $GS_i^{(1,1)} = \frac{z_{e,d}}{d_{1_d}}$

(d) $S_o^{(1,1)} = \frac{z_{e,d}}{d_{2_d}}$
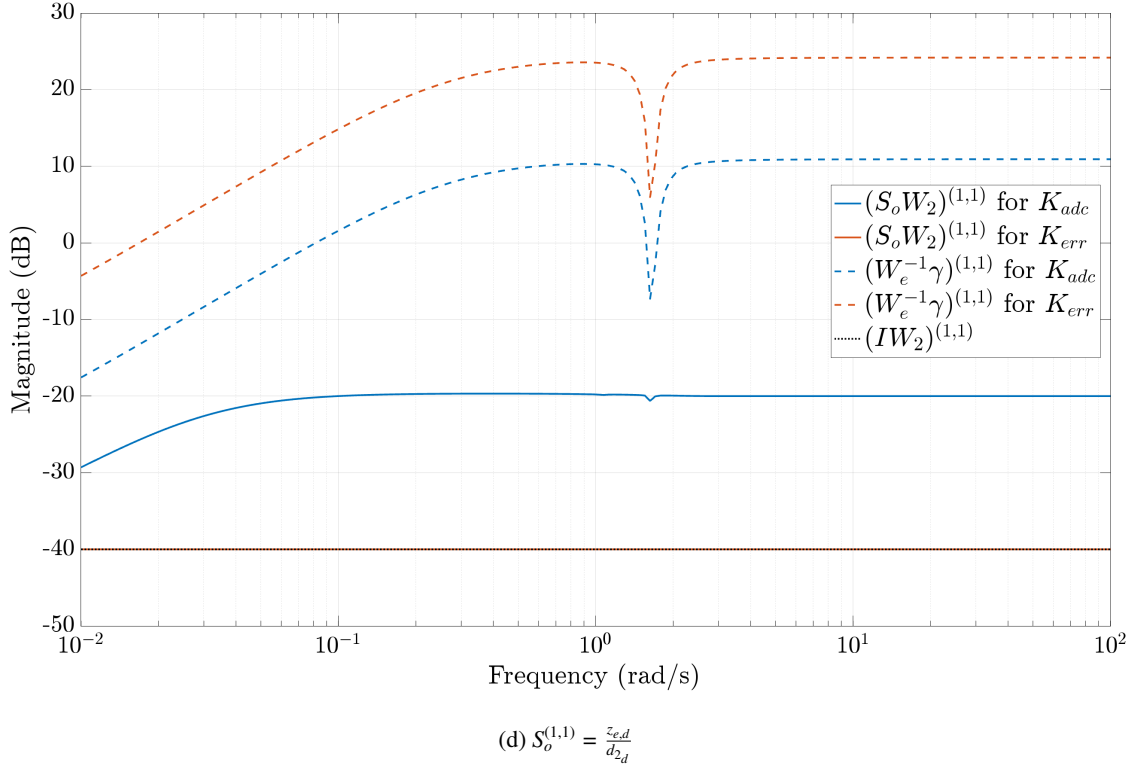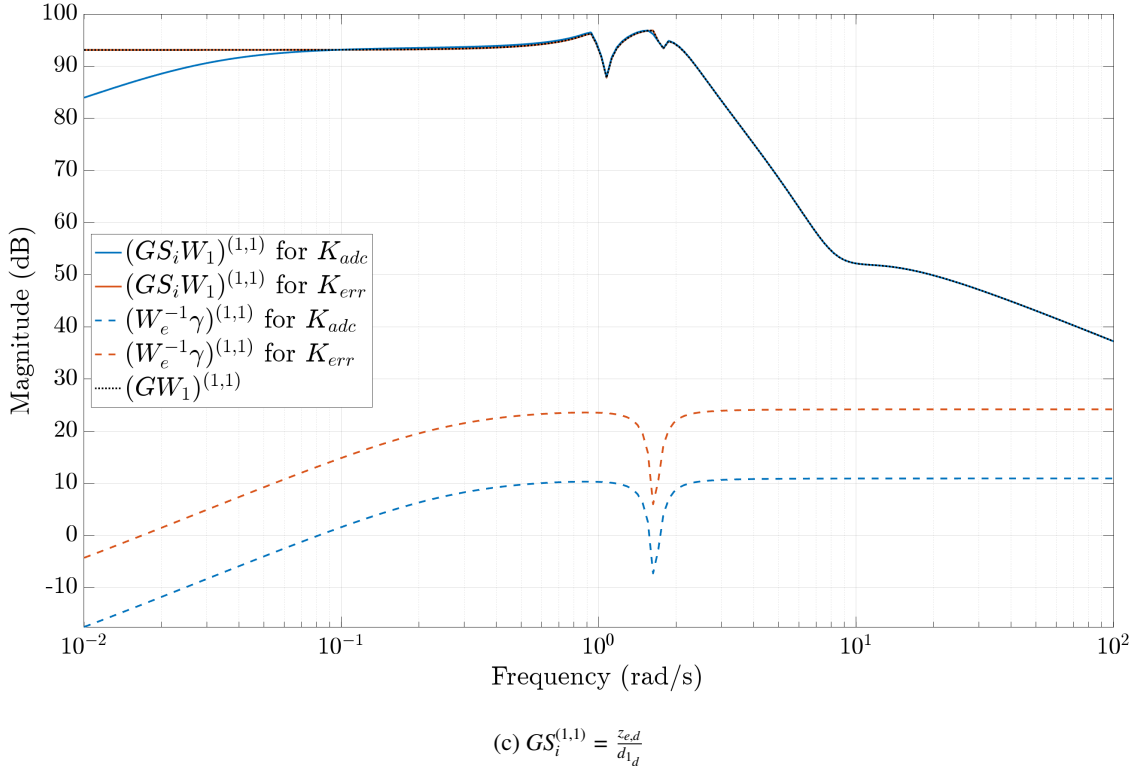
FIGURE 9 $d-d$ channel of transfer functions resulting from K_{adc} controller (blue) and K_{err} controller (red), tuned with wind turbine model linearized at 16 m/s, bounded by $W_1^{-1}\gamma$ and $W_2^{-1}\gamma$ (dashed, colored blue and red for K_{adc} and K_{err}, respectively), with open-loop cases for GS_i (open-loop plant, G) and S_o (identity function, I) (black, dotted).

multi-loop output disk margins by injecting independent perturbations at all outputs to the plant if we wish to estimate the corresponding uncertainty at the plant outputs, or in the most conservative case we could estimate the *multi-loop input/output disk margin* by injecting independent perturbations at all plant input and outputs.

The left plots of Fig. 10 show the variation in the gain and phase components of worst-case loop-at-a-time disk margins (i.e. the worst loop-at-a-time disk margin over all $d-d$, $d-q$, $q-d$ and $q-q$ channels) for K_{adc} and K_{err} controllers tuned with a range of A_{W_u} values and wind turbine plants linearized at 12, 14, 16, 18, 20 and 22 m/s. The right plots show the equivalent variation for the multi-loop input/output disk margins. We can see that the gain and phase components of the multi-loop disk margin, the most conservative robustness metric shown, tend to be greater for K_{adc} controllers and also to increase with A_{W_u}. There is a small reduction in robustness for controllers tuned with plants linearized at 14-22 m/s, but it does not appear to be significant. We cannot draw as clear a conclusion from the worst case loop-at-a-time disk margin plots, for which there is not a significant difference in robustness between K_{adc} and K_{err} controllers and no general trend across linearizing wind-speeds or values of A_{W_u}, although controllers tuned at 18 m/s do appear to be less robust than the others for high values of A_{W_u} in particular. This highlights the importance of inspecting several metrics to investigate robustness. Note that, while we have studied the robustness of controllers tuned for plants linearized at a range of wind speeds here, in this work we only implement those based on a plant linearized at 16 m/s for nonlinear analysis. In future work, we intend to investigate the potential improvements in using a gain-scheduled controller that utilizes controllers tuned across a range of wind speeds and interpolates between the resulting IPC signals as the incoming wind speed changes.
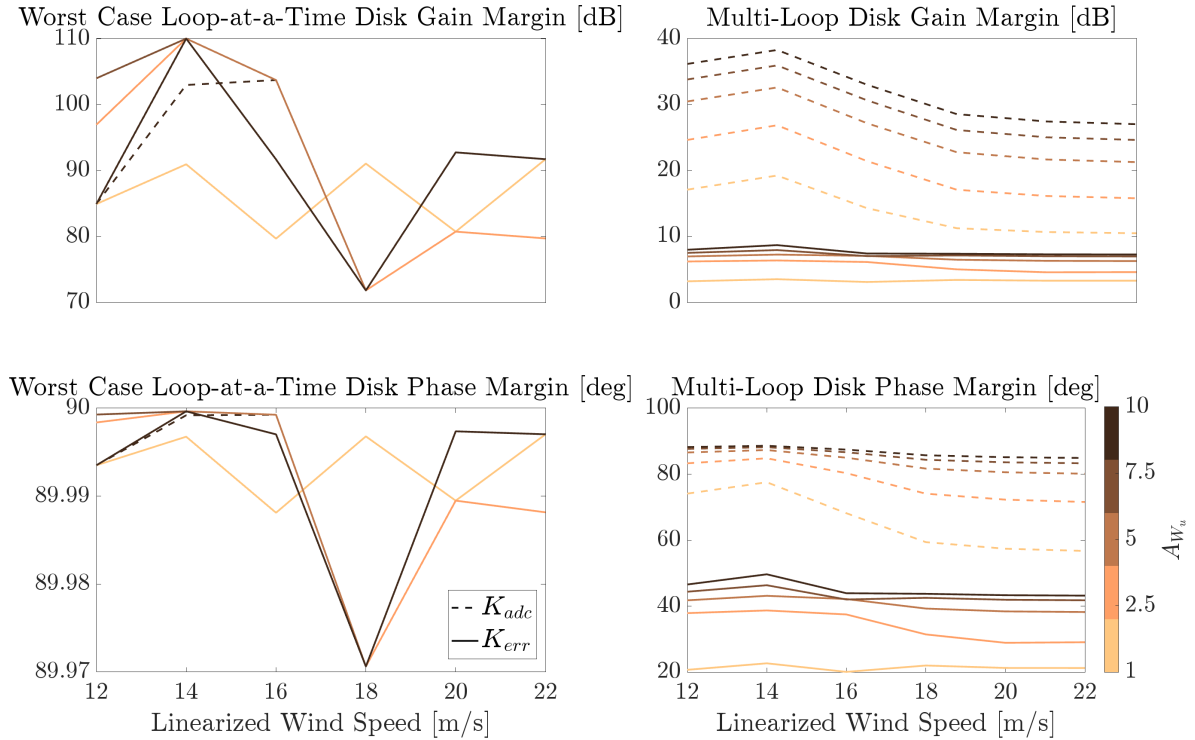
FIGURE 10 Robust stability margins for K_{err} (solid line) and K_{adc} (dashed line) for increasing values of the gain A_{W_u} (darker colors corresponding to higher A_{W_u}).

5 | NONLINEAR ANALYSIS

In order to more fully evaluate the performance and actuator activity of the tuned controllers, we run closed-loop simulations on a model of the SUMR[7] wind turbine using the open-source aero-servo-hydro-elastic wind turbine simulation tool OpenFAST.[34]

Since the objective of the IPC controllers is to mitigate $0P$ and $3P$ loads in the non-rotating domain, the wind fields used in the simulation studies are designed to incur these loads by including a high wind shear (causing an asymmetrical load on the rotor that induces tilting, or d-axis moments) and high turbulence. TurbSim[35] is used to generate 600-second time-series of turbulent wind fields at mean wind speeds of 12, 14, 16, 18, 20, 22 m/s ($R3$ in Fig. 1), for 5 different seeds, with a Normal Turbulence Model (NTM) of Class A turbulence intensity and a wind shear exponent of 0.2. In this section, we discuss the frequency content of the loads measured in terms of the power spectral density (PSD) of the loads under inspection at the frequencies of interest and the DELs and the actuator activity resulting from these nonlinear simulations. The measured change in PSD peaks and DELs for loads of interest are averaged over all wind field seeds for each controller implementation tested. We compare these metrics for the best-performing $\mathcal{H}_\infty$-synthesized controllers for each of three ADC attenuation techniques tested: retuning with greater A_{W_u} values, nonzero reference values for M_d, and finite saturation values for $[\beta_1^{ipc}, \beta_2^{ipc}, \beta_3^{ipc}]$.

5.1 | Power Spectral Densities (PSDs) of Loads

The *power spectral density* [dB/Hz] of a time-series signal measures the power present in the signal at every frequency per unit of frequency. The purpose of the tuned IPC controllers is to reduce the loads at $0P$ and $3P$ frequencies in the non-rotating domain, corresponding to $1P$ and $2P$ frequencies in the rotating domain. We would expect then to see a reduction in the power of relevant non-rotating loads at $0P$ and $3P$ frequencies and in the power of rotating loads at $1P$ and $2P$ frequencies. Fig. 11 shows the percentage change, relative to the open-loop case, in the out-of-plane blade-root bending moment (a rotating load) at $1P$ and $2P$ frequencies (left plots) and in the tower-top tilt and yaw (i.e. in the d and q coordinates, respectively) bending moment (non-rotating loads) at $0P$ and $3P$ frequencies (middle and right plots, respectively), for the range of mean wind speeds of the turbulent wind fields used in the nonlinear simulations.

Note that all IPC controllers result in a reduction in the $1P$ and $2P$ blade-root bending moments. This is to be expected, as a) it is the tracking error of this load (MBC-transformed into the non-rotating domain) that is read as an input to the controllers and b) all controllers, including the baseline (blue), K_0, target the $0P$ loads in the transformed domain, which corresponds to this $1P$ rotating load. However, it is only the tuned controllers (red, yellow, and purple, not including the baseline case), which result in $2P$ reductions in the blade-root bending moment and $0P$ reductions of the non-rotating loads for all mean wind speeds. For mean wind speeds of 14 m/s and greater, all tuned controllers achieve approximately 80% reductions in the $1P$ blade-root bending moment and $0P$ tower-top tilt and yaw bending moments.

Considering the $2P$ rotating load and $3P$ non-rotating loads (bottom plots), the tuned controllers result in a reduction in the moments for all mean wind speeds, ranging between 20% to 45% for all loads and mean wind speeds (except for 14 m/s in the tower-top tilt bending moment case, which still presents a reduction of approximately 10%). The retuning technique in particular is consistently superior or as good as the other tuned controllers, in terms of $3P$ tower-top yaw bending moment reductions.

Fig. 12 compares the full PSD of the open-loop, baseline, and best-performing (in terms of PSD reductions at critical frequencies, averaged over all loads/frequencies of interest) controller from the retuning set for a simulation with a mean wind speed of 16 m/s. As expected, we can see that the rotating load (top plot) shows reduced peaks at $1P$ and $2P$ for the tuned controller, and reductions at $0P$ and $3P$ for the non-rotating loads (middle and bottom plots).

5.1.1 | Damage Equivalent Loads (DELs)

The *damage-equivalent load* metric for each wind turbine component is an estimate of the constant amplitude periodic load, that if applied to a given wind turbine over its operating lifetime, would result in an accumulated damage equal to that caused by the stochastic wind field loading over the same lifetime.[36] It is computed by applying a rainflow counting algorithm to a collection of nonlinear simulations conducted for wind conditions of interest.[37]

Fig. 13 shows the percentage change in DELs relative to the open-loop case for different rotating (out-of-plane blade-root bending moment) and non-rotating (tower-top tilt and yaw bending moment) loads for the baseline IPC controller (blue) and the best-performing (in terms of greatest DEL reduction) tuned full-order controllers using the A_{W_u} retuning (red), nonzero output reference (yellow), and finite control input saturation (purple) techniques to penalize actuator activity at each mean wind speed. It also shows the equivalent change for ADC for the baseline and tuned cases (top-right plot). Note that the left y-axis corresponds to the baseline (blue) controller, while the right y-axis corresponds to the tuned (red, yellow and purple) controllers.
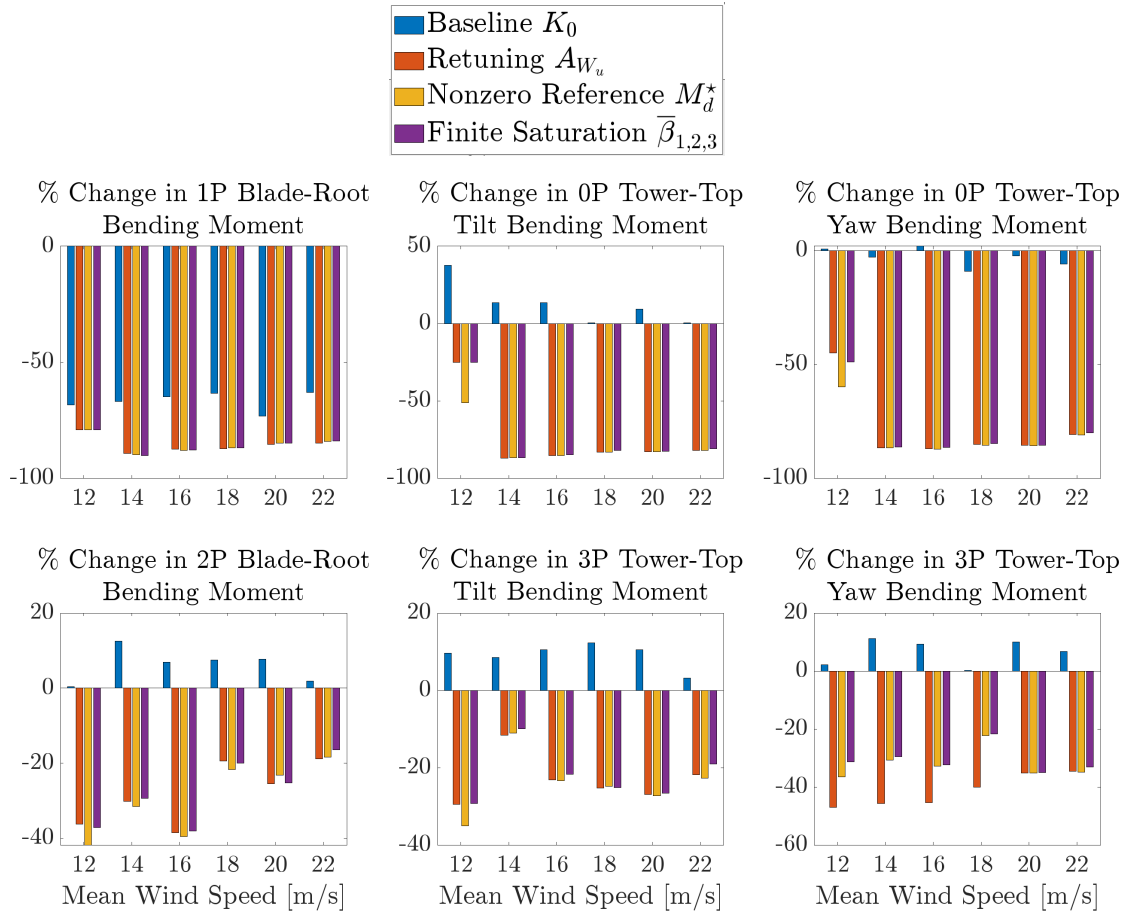
FIGURE 11 Percentage change in PSD at frequencies of interest for different rotating and non-rotating loads for baseline and best-performing controllers (in terms of mean PSD reduction over all loads and frequencies of interest) generated from the baseline (blue), retuning (red), nonzero reference (yellow), and finite saturation (purple) techniques, averaged over 5 seeds of turbulent wind fields with varying mean wind speeds.

We can see that all controllers result in a reduction in the DEL for the blade-root bending moment, with all three tuned controllers achieving the greatest reduction of up to $5 - 7\%$ in the case of the 22 m/s mean wind speed. The results for the tower-top tilt bending moment DEL are more ambiguous, varying over mean wind speeds, with the tuned controllers sometimes presenting *increases* of up to 16%, although this is notably less than the corresponding increases for the baseline case over most mean wind speeds. Looking at the change in DELs for the tower-top yaw bending moment, we see that only the tuned controllers result in negligible changes, whereas the baseline controller incurs $5 - 10\%$ increases for all mean wind speeds. It would appear that reductions in the frequencies of interest, namely $0P$ and $3P$, in the non-rotating domain using the blade-root bending moment tracking error as an input to the controller are likely to result in reductions in power spectral density (PSD) at these frequencies, but that this may not translate to reductions in the DELs associated with non-rotating components (tower-top tilt and yaw bending moments).

5.2 | Actuator Activity Analysis

A secondary objective of the IPC controllers designed in this work is to limit the actuator activity, or ADC, of the blade-pitch actuators. Note that ADC will always increase with the implementation of an IPC controller relative to the open-loop case, but that we would like to keep this value to the minimum necessary to achieve our load attenuation objectives. The top right plot in Fig. 13 shows that the baseline case results in the greatest increase of up to 500% in ADC relative to the open-loop case,
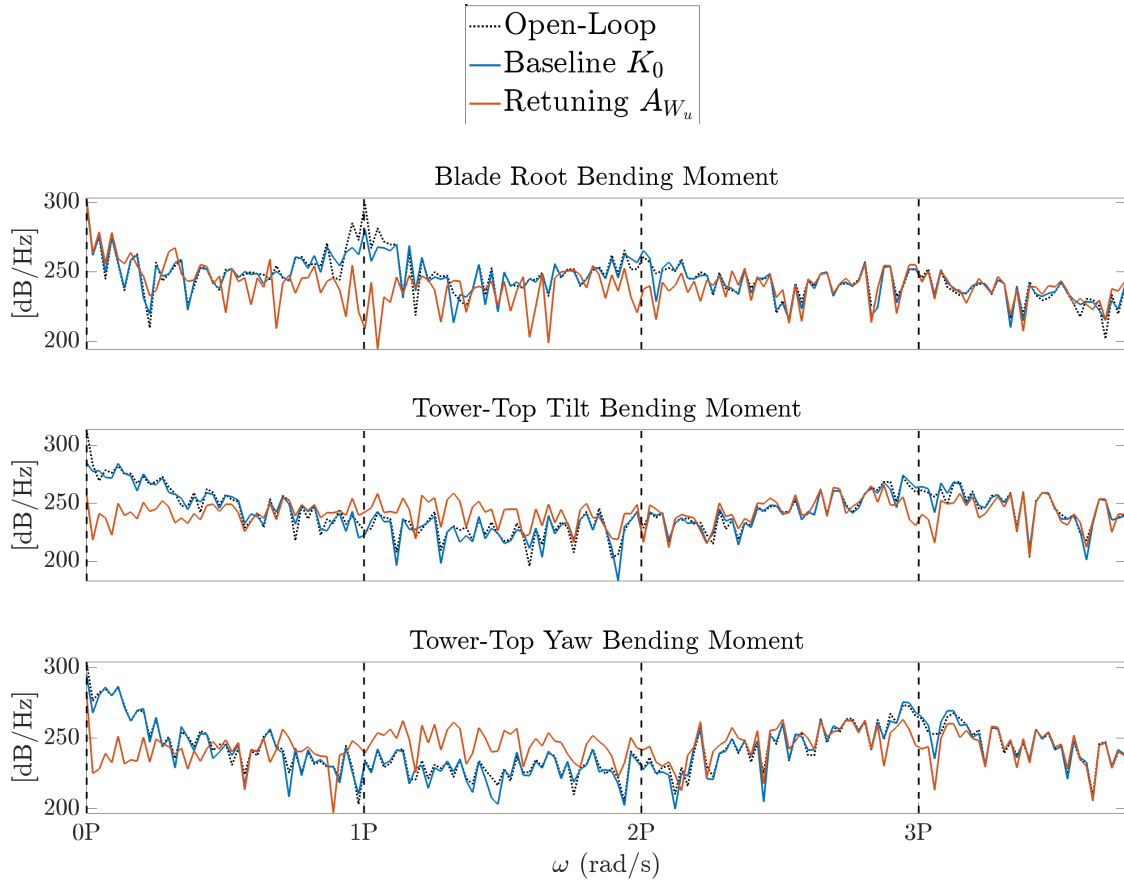
FIGURE 12 PSD of open-loop (dotted, black), baseline (blue, solid), and best-performing (in terms of mean PSD reduction over all loads under inspection) tuned controllers (red, solid) for retuning technique of different loads under a sample turbulent wind field with mean wind speed of 16 m/s

compared to increases of less than 4% for all tuned controllers. The retuning technique results in the greatest ADC attenuation, while the finite saturation technique results in the least attenuation, although it is still significantly superior to the baseline case.

Fig. 14 shows the time-series variation in the blade-pitch angle (the sum of the collective and individual pitch control commands), β_1, and the its rate of change, $\frac{d\beta_1}{dt}$, for blade 1 over a single rotation of the rotor (corresponding to a 360° revolution of the azimuth angle, θ, in the top plot), for the baseline (blue) controller and controllers generated from the retuning (red), nonzero reference (yellow), and finite saturation (purple) techniques. Looking at the β_1 (middle) plot, we see that the baseline, retuning, and nonzero reference controllers all result in IPC signals that are in phase, with the greatest amplitude for the retuned controller and least amplitude for the baseline controller. In contrast, the IPC signal for the finite saturation case seems to be out-of-phase with the others, showing how saturation can impact the shape of the control input waveform necessary to mitigate periodic load signals. The rate-of-change in the actuation signal, $\frac{d\beta_1}{dt}$ (bottom plot) presents noise in the case of the baseline controller whereas the tuned controllers are smoother. All three tuned controllers are well within the blade-pitch rate-of-change bounds of $[-4, 5]°$/s imposed on the turbine.

6 | CONCLUSIONS

In conclusion, it is found that all three implementations of $\mathcal{H}_\infty$-synthesized multivariable controllers with ADC mitigation techniques are superior in terms of PSD attenuation of rotating and non-rotating loads at targeted frequencies, DEL reduction of rotating loads and ADC mitigation, compared to the baseline SISO PI controller.
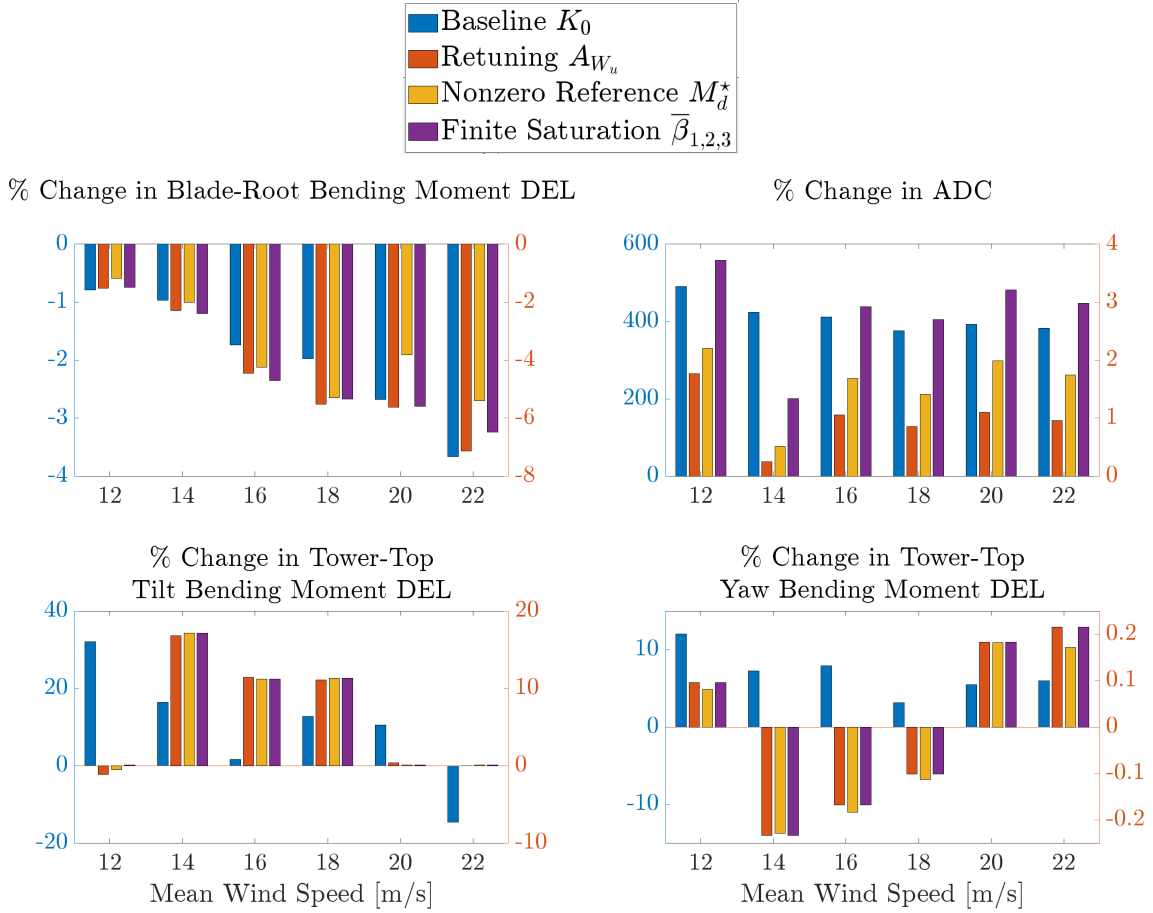
FIGURE 13 Percentage change in DELs and ADCs under turbulent wind fields with mean wind speeds of 12, 14, 16, 18, 20, 22 m/s for baseline, and best-performing controllers for varying A_{W_u}, varying $M_d^\star$ and $\overline{\beta}_1$ cases (in terms of greatest decrease or least increase in DEL and ADC relative to open-loop case)

A reduction of approximately 80% is achieved for the $1P$ out-of-plane blade-root and $0P$ tower-top tilt and yaw bending moments for all mean wind speeds included in the set of turbulent wind fields run in simulation; and a reduction of approximately 20-45% is achieved for the $2P$ out-of-plane blade-root bending moment and $3P$ tower-top tilt and yaw bending moments for all mean wind speeds.

In terms of limiting ADC, the retuning approach proves to result in the least increase relative to the open-loop case across all mean wind speeds run in simulation. We can conclude that all three methods succeed in significantly reducing ADC compared to the baseline case, with increases of less than 4% compared to 500% in the baseline case. It is found, however, that the retuning approach is the most effective, achieving increases of less than 2% for all mean wind speeds. The study of the controllers synthesized for a sweep of weighting functions gains suggests that the controller that induces the lowest ADC is also the most robust controller in terms of multi-loop disk margin.

It is noteworthy that while a tuned controller may perform well in terms of PSD attenuation, that this does not necessarily translate to reduction in DELs for the same components. This may be a result of additional harmonics present in the loads beyond $0P$ and $3P$, or it may be that the IPC actuator activity introduces additional fatigue. Nonetheless, the tuned controllers do result in the greatest decreases in DELs associated with the out-of-plane blade-root bending moment ranging from $2 - 7\%$ for different mean wind speeds run in simulation, compared to decreases of approximately $0.5 - 3.5\%$ for the baseline controller.

Further investigation of the $\mathcal{H}_\infty$-tuned IPC presented in this work is warranted to fine-tune the performance and to thoroughly test it. Some goals for future work include:
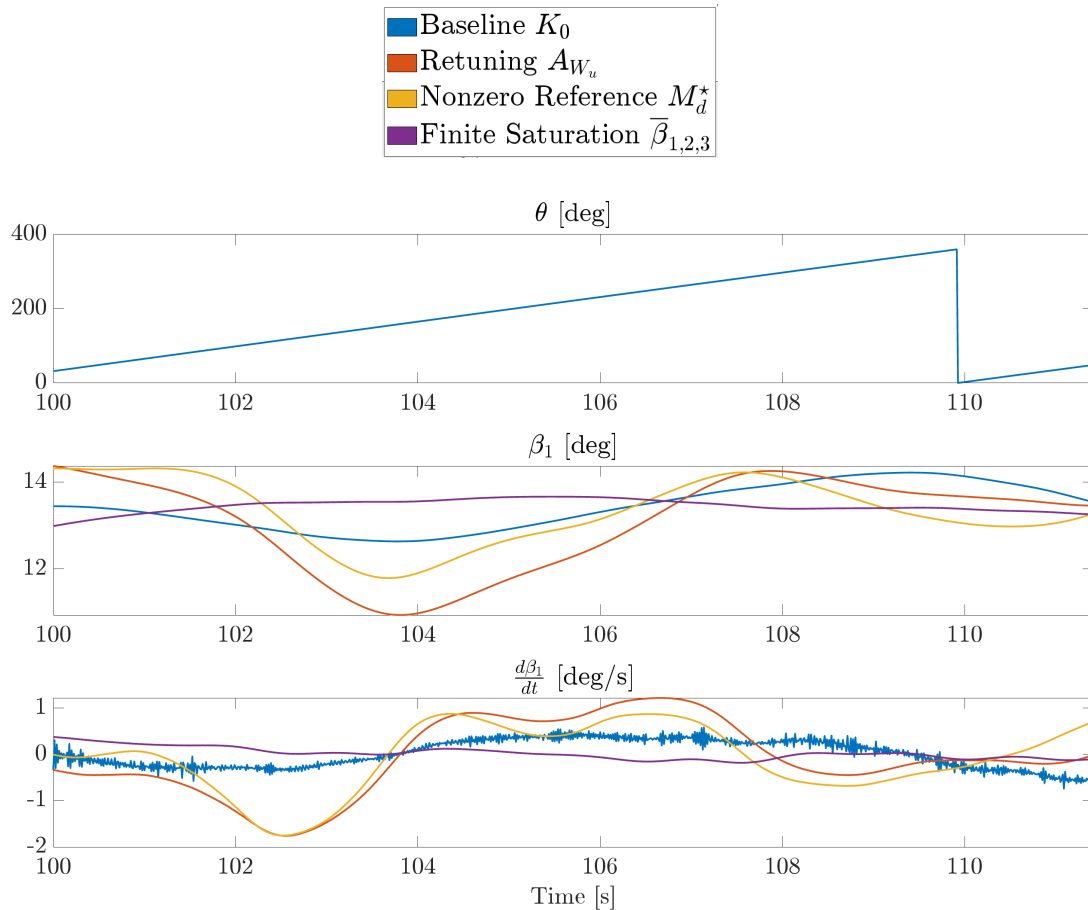
FIGURE 14 Time-series plot of θ, β_1, $\frac{d\beta_1}{dt}$ under turbulent wind field with mean wind speed of 16 m/s for baseline and tuned controllers for retuning, nonzero reference, and finite saturation techniques

- Investigation into the reason that tuned controllers succeed in reducing PSDs at targeted frequencies but fail to achieve the same significant reductions in DELs of non-rotating components.
- Tuning a multivariable structured controller, such as a series combination of PI regulators and inverse notch filters, that approximates the optimized full-order controller via $\mathcal{H}_\infty$-synthesis.
- Comparing the performance, robustness, and actuator activity of a controller tuned at a single wind speed with a gain-scheduled controller tuned at several wind speeds.
- Validating the tuned controllers on a scaled test wind turbine.
- Open-source release of a user-friendly framework for the purposes of auto-tuning IPCs for any given wind turbine model.

REFERENCES

1. Barlas TK, van Kuik GA. Review of state of the art in smart rotor control research for wind turbines. *Progress in Aerospace Sciences*. 2010;46(1):1–27.
2. Bossanyi EA. Individual blade pitch control for load reduction. *Wind Energy: An International Journal for Progress and Applications in Wind Power Conversion Technology*. 2003;6(2):119–128.
3. Zhang Y, Chen Z, Cheng M. Proportional resonant individual pitch control for mitigation of wind turbines loads. *IET Renewable Power Generation*. 2013;7(3):191–200.
4. Bir GS. User's guide to MBC3: Multi-blade coordinate transformation code for 3-bladed wind turbine. 2010.
5. Pao LY, Johnson KE. A tutorial on the dynamics and control of wind turbines and wind farms. *American Control Conference*. 2009:2076–2089.
6. Abbas NJ, Zalkind DS, Pao L, Wright A. A reference open-source controller for fixed and floating offshore wind turbines. *Wind Energy Science*. 2022;7(1):53–73.
7. Mendoza ASE, Griffith DT, Qin C, Loth E, Johnson N. Rapid approach for structural design of the tower and monopile for a series of 25 MW offshore turbines. *Journal of Physics: Conference Series*. 2022;2265(3):032030.

8. Bossanyi E. Wind turbine control for load reduction. *Wind Energy: An International Journal for Progress and Applications in Wind Power Conversion Technology*. 2003;6(3):229–244.

9. Bossanyi EA, Fleming PA, Wright AD. Validation of Individual Pitch Control by Field Tests on Two- and Three-Bladed Wind Turbines. *IEEE Transactions on Control Systems Technology*. 2013;21(4):1067-1078. doi: 10.1109/TCST.2013.2258345

10. van Engelen T, van Der Hooft E. Individual pitch control inventory. *Technical Report ECN-C-03-138*. 2005.

11. van Engelen T. Design model and load reduction assessment for multi-rotational mode individual pitch control (higher harmonics control). 2006.

12. Bottasso CL, Campagnolo F, Croce A, Tibaldi C. Optimization-based study of bend–twist coupled rotor blades for passive and integrated passive/active load alleviation. *Wind Energy*. 2013;16(8):1149–1166.

13. Petrović V, Jelavić M, Baotić M. MPC framework for constrained wind turbine individual pitch control. *Wind Energy*. 2021;24(1):54–68.

14. Friis J, Nielsen E, Bonding J, Adegas FD, Stoustrup J, Odgaard PF. Repetitive model predictive approach to individual pitch control of wind turbines. *2011 50th IEEE Conference on Decision and Control and European Control Conference*. 2011:3664–3670.

15. Raach S, Schlipf D, Sandner F, Matha D, Cheng PW. Nonlinear model predictive control of floating wind turbines with individual pitch control. *2014 American control conference*. 2014:4434–4439.

16. Mirzaei M, Soltani M, Poulsen NK, Niemann HH. An MPC approach to individual pitch control of wind turbines using uncertain LIDAR measurements. *2013 European Control Conference*. 2013:490–495.

17. Selvam K, Kanev S, van Wingerden JW, van Engelen T, Verhaegen M. Feedback–feedforward individual pitch control for wind turbine load reduction. *International Journal of Robust and Nonlinear Control: IFAC-Affiliated Journal*. 2009;19(1):72–91.

18. Nourdine S, Camblong H, Vechiu I, Tapia G. Comparison of wind turbine LQG controllers using individual pitch control to alleviate fatigue loads. *18th Mediterranean Conference on Control and Automation*. 2010:1591–1596.

19. Camblong H, Nourdine S, Vechiu I, Tapia G. Comparison of an island wind turbine collective and individual pitch LQG controllers designed to alleviate fatigue loads. *IET Renewable Power Generation*. 2012;6(4):267–275.

20. Han Y, Leithead W. Combined wind turbine fatigue and ultimate load reduction by individual blade control. *Journal of Physics: Conference Series*. 2014;524(1):012062.

21. Leithead W, Neilson V, Dominguez S. Alleviation of unbalanced rotor loads by single blade controllers. *Wind Energy Conference & Exhibition*. 2009.

22. Castaignet D, Couchman I, Poulsen NK, Buhl T, Wedel-Heinen JJ. Frequency-weighted model predictive control of trailing edge flaps on a wind turbine blade. *IEEE Transactions on Control Systems Technology*. 2013;21(4):1105–1116.

23. Castaignet D, Barlas T, Buhl T, et al. Full-scale test of trailing edge flaps on a Vestas V27 wind turbine: active load reduction and system identification. *Wind Energy*. 2014;17(4):549–564.

24. Andersen PB, Henriksen L, Gaunaa M, Bak C, Buhl T. Deformable trailing edge flaps for modern megawatt wind turbine controllers using strain gauge sensors. *Wind Energy: An International Journal for Progress and Applications in Wind Power Conversion Technology*. 2010;13(2-3):193–206.

25. Andersen PB. Advanced load alleviation for wind turbines using adaptive trailing edge flaps: sensoring and control. 2010.

26. Geyler M, Caselitz P. Robust multivariable pitch control design for load reduction on large wind turbines. *Journal of solar energy engineering*. 2008;130(3).

27. Lu Q, Bowyer R, Jones BL. Analysis and design of Coleman transform-based individual pitch controllers for wind-turbine load reduction. *Wind Energy*. 2015;18(8):1451–1468.

28. McFarlane D, Glover K. A loop-shaping design procedure using $\mathcal{H}_\infty$ synthesis. *IEEE Transactions on Automatic Control*. 1992;37(6):759–769.

29. Skogestad S, Postlethwaite I. *Multivariable feedback control: analysis and design*. John Wiley & sons, 2005.

30. Ossmann D, Theis J, Seiler P. Robust control design for load reduction on a Liberty wind turbine. *Dynamic Systems and Control Conference*. 2016;50695:V001T04A002.

31. Ossmann D, Theis J, Seiler P. Load reduction on a Clipper Liberty wind turbine with linear parameter-varying individual blade pitch control. *Wind Energy*. 2017;20(10):1771–1786.

32. Ossmann D, Seiler P, Milliren C, Danker A. Field testing of multi-variable individual pitch control on a utility-scale wind turbine. *Renewable Energy*. 2021;170:1245–1256.

33. Vali M, van Wingerden JW, Kühn M. Optimal multivariable individual pitch control for load reduction of large wind turbines. *American Control Conference*. 2016:3163–3169.

34. Working with OpenFAST documentation. https://ebranlard-openfast.readthedocs.io/en/doc/source/working.html; 2022. [Online; accessed 20-August-2022].

35. Jonkman BJ. TurbSim user's guide: Version 1.50. tech. rep., National Renewable Energy Lab (NREL), Golden, CO (United States); 2009.

36. Freebury G, Musial W. Determining equivalent damage loading for full-scale wind turbine blade fatigue tests. *ASME Wind Energy Symposium*. 2000:50.

37. Gasch R, Twele J. *Wind power plants: fundamentals, design, construction and operation*. Springer Science & Business Media, 2011.